electronics

MDPI

Review

From Wave Manipulation to Programmable Apertures: A Review of Metasurface-Enabled Radar

Fanglin Geng, Liguo Liu *, Beibei Zhang, Kun Zhao and Qingyi Zhang

School of Electronic Engineering, Naval University of Engineering, Wuhan 430033, China; 2520252087@nue.edu.cn (F.G.); 1920191211@nue.edu.cn (B.Z.); m25181013@nue.edu.cn (K.Z.); 2420242015@nue.edu.cn (Q.Z.)

* Correspondence: 1309021015@nue.edu.cn

Abstract

Electromagnetic wave manipulation underpins radar detection, imaging, and electronic countermeasures. Conventional phased-array and radio-frequency-chain-based radar architectures provide mature and high-performance operation but can face practical constraints related to aperture profile, power and thermal management, calibration, bandwidth, and multifunctional integration. Electromagnetic metasurfaces provide a complementary approach by controlling the phase, amplitude, polarization, and frequency content of scattered or radiated fields through subwavelength surface elements. This article presents a radar-system-oriented review of metasurface-enabled wave manipulation. We first summarize the relevant physical mechanisms, including generalized scattering, digital and information metasurfaces, time-varying modulation, and polarization and geometric-phase control. We then review experimentally reported applications in radar-cross-section control, programmable beam steering, computational imaging, time-modulated radar, multiple-input multiple-output systems, and integrated sensing and communication. Particular attention is given to the level of experimental validation and to the distinction between measured device- or subsystem-level performance and anticipated system-level benefits. Potential applications in stealth, radar deception, low-probability-of-intercept-oriented operation, and cognitive sensing are discussed together with limitations in bandwidth, efficiency, power handling, biasing, calibration, thermal management, and scalability. Overall, the available literature indicates that metasurfaces can support selected aperture-level radar functions, whereas general system-level advantages in SWaP, cost, latency, and energy efficiency remain to be established through controlled comparative experiments.

Keywords: electromagnetic metasurfaces; radar wave manipulation; radar cross-section; programmable beam steering; spatiotemporal modulation; integrated sensing and communications

Check for updates

Academic Editor: Toshifumi Moriyama

Received: 15 May 2026
Revised: 5 August 2026
Accepted: 7 August 2026
Published: 12 August 2026

Copyright: © 2026 by the authors. Licensee MDPI, Basel, Switzerland. This article is an open access article distributed under the terms and conditions of the Creative Commons Attribution (CC BY) license.

1. Introduction

Electromagnetic wave manipulation has long served as the core driving force for advances in radar detection, imaging, and electronic countermeasure (ECM) functions [1–3]. Since World War II, radar systems have undergone multiple technological paradigm shifts, evolving from mechanically scanned antennas and passive electronically scanned arrays to active electronically scanned arrays (AESAs). All these transformative leaps fundamentally originate from continuous progress in electromagnetic wave manipulation across spatial, temporal, and spectral domains [4,5]. Nevertheless, driven by surging system integration

and functional complexity, conventional radar architectures built on radio-frequency (RF) chains and phased arrays are gradually hitting performance ceilings constrained by inherent hardware limitations [6].

Recent advances in broadband low-profile antenna arrays, represented by miniaturized antipodal Vivaldi antenna arrays, have boosted the overall performance and system integration level of traditional antenna structures. Yet, such antenna technologies still rely on fixed pre-designed radiation layouts and cannot deliver the dynamic electromagnetic reconfigurability characteristic of metasurfaces [7].

In complex modern electromagnetic environments, radar systems face a set of increasingly stringent, interdependent performance requirements, including wide instantaneous bandwidth, rapid beam-steering agility, parallel multi-task processing, and reliable target detection under severe electronic countermeasure scenarios [8]. Furthermore, strict size, weight, and power (SWaP) constraints borne by airborne, spaceborne, and missile-borne platforms greatly complicate the trade-off between system performance, architectural design, and engineering practicability [9]. Although mainstream architectures represented by AESAs deliver outstanding performance via high-density transmit/receive modules, they are plagued by bulky hardware layouts, excessive power dissipation, severe thermal management difficulties, and complicated calibration workflows, which place severe restrictions on system scalability and deployment flexibility [5]. Moreover, as competition over limited spectrum resources grows fiercer among radar, communication, and electronic warfare systems, traditional radar apertures optimized for single missions fail to satisfy the requirements for high-freedom beam reconfiguration and multi-task multiplexing demanded by emerging frameworks including ISAC and cognitive radar [10,11].

From the perspective of scattering regulation and stealth technology, conventional radar cross-section (RCS) reduction techniques mainly adopt geometric profiling optimization and radar-absorbing materials (RAMs) [12]. However, these two schemes are inherently restricted by physical mechanisms and engineering drawbacks: shape-based stealth places severe restrictions on aerodynamic configuration and structural design, while conventional absorbing materials suffer from thickness bottlenecks at low frequencies, which makes it hard to simultaneously realize lightweight design and broadband absorption performance [13]. More critically, nearly all these stealth strategies lack dynamic reconfigurability and thus fail to adapt to the evolving trends of complex radar systems with multi-band, multi-polarization, and multistatic cooperative detection capabilities. Therefore, it is urgent to explore an innovative electromagnetic interface capable of dynamic manipulation of scattering signatures while retaining lightweight structural features [14].

Electromagnetic metasurfaces provide a potential solution to address the aforementioned challenges [15–17]. As two-dimensional artificial electromagnetic interfaces constructed from subwavelength unit cells, metasurfaces achieve precise control of electromagnetic scattering by introducing spatially inhomogeneous phase discontinuities at the material interface [15,18]. Unlike conventional devices that rely on phase accumulated along propagation paths, metasurfaces reconstruct wavefronts directly at deep subwavelength scales via equivalent surface impedance or polarization responses. Moreover, they support joint control over amplitude, polarization, and spectrum dimensions [16,19]. Early investigations mainly focused on static analog metasurfaces such as phase-gradient metasurfaces and transmitarrays. Their electromagnetic responses remain fixed once fabricated, which cannot satisfy radar requirements for real-time reconfiguration and multi-task switching [18]. In recent years, with the integration of digital coding theory and active components (e.g., PIN diodes, varactors, and MEMS switches), metasurfaces have evolved into programmable information-driven electromagnetic apertures. Further enabled by spatiotemporal modulation, linear time-varying metasurface systems are realized to deliver unique

functions including spectral reshaping and Doppler modulation [20–23]. This technical shift transforms electromagnetic manipulation from "structure-defined" to "information-defined", creating an innovative implementation paradigm for radar systems that differs fundamentally from conventional RF front-end chains [21,24].

Recent research advances further verify that metasurfaces are developing into integrated apertures with multifunctionality, polarization multiplexing, ultrawideband response and space–time programmability. For instance, 3D-printed polarization-division multiplexed metadevices have been reported to realize multifunctional wavefront reshaping for radar applications. Meanwhile, emerging low-profile ultrawideband aperture designs highlight the necessity of broadband and compact integration schemes for radar-dedicated platforms. In parallel, space–time-coding metasurfaces enable simultaneous spatial- and frequency-domain electromagnetic modulation, opening new avenues for harmonic beam regulation, custom waveform generation, and integrated radar and communication systems. In contrast to existing review articles focused merely on metasurface physical fundamentals, programmable electromagnetic structures, information-coding metasurfaces, RIS-aided wireless communications, dynamic metasurface antennas, or isolated radar application scenarios, this review is structured along the full radar system workflow, covering electromagnetic modulation mechanisms, aperture functionalities, and practical engineering deployment constraints. Rather than proposing a brand-new metasurface device, this work comprehensively summarizes how various metasurface modulation mechanisms underpin core radar capabilities, including RCS suppression, programmable beamforming, radar imaging, time-domain modulation, MIMO, ISAC, LPI operation, and cognitive sensing. We place special emphasis on the technical gap between laboratory prototypes and practically deployable radar systems. As summarized in Table 1, prior reviews have provided comprehensive treatments of metasurface tuning mechanisms, software-defined control, space–time coding, and RCS-reduction techniques. Nevertheless, their organizing frameworks are predominantly centered on materials, electromagnetic functions, coding principles, or target-side stealth. The present review differs by treating the metasurface as a functional component within a radar system and by tracing the complete relationship from physical reconfiguration to electromagnetic response, radar architecture, signal-processing function, experimental validation, and reported system performance.

This work serves as a comprehensive integrative review rather than a rigorous systematic review. We select literature covering representative and influential studies on radar wave manipulation and programmable apertures empowered by electromagnetic metasurfaces. Relevant articles are retrieved from mainstream academic databases and publishing platforms, including Web of Science, Scopus, IEEE Xplore, ScienceDirect, SpringerLink, and Google Scholar, with the following search keywords: "metasurface radar", "programmable metasurface", "coding metasurface", "reconfigurable aperture", "RCS reduction", "metasurface beamforming", "dynamic metasurface antenna", "time-varying metasurface", "MIMO radar", and "ISAC". We prioritize publications that elaborate distinct electromagnetic mechanisms, radar-specific functions, experimental validations, or discussions on practical engineering deployment. All screened studies were organized along the complete technical thread: fundamental physical mechanisms, radar functional implementations, and practical engineering bottlenecks.

Table 1. Comparison of the present review with representative prior reviews on reconfigurable, intelligent, and radar-related metasurfaces.

Representative Review	Publication Year	Principal Scope	Radar-Related Coverage	Scope Boundary Relative to the Present Review
Tsilipakos et al. [25]	2020	Evolution from globally tunable metasurfaces to software-defined metasurfaces incorporating distributed sensing, actuation, processing, and embedded controller networks.	Introduces intelligent electromagnetic environments and discusses general communication, sensing, and imaging opportunities.	Primarily establishes intelligent-metasurface architectures and control concepts; radar-system positions, radar signal-processing functions, and quantitative radar demonstrations are not its principal organizing framework.
Murugesan et al. [26]	2021	Conventional and metasurface-assisted radar-cross-section reduction, including scattering, absorption, passive and active configurations, bandwidth, angular stability, and polarization sensitivity.	Provides detailed coverage of target-side radar stealth and electromagnetic-scattering reduction.	Concentrates on reducing target observability; reconfigurable radar transmitters, receiving apertures, waveform generation, RF preprocessing, computational imaging, and system-level radar integration are outside its principal scope.
Zhang and Cui [27]	2021	Principles of space–time-coding digital metasurfaces, harmonic generation, spectral–spatial manipulation, programmable nonreciprocity, and representative information-processing applications.	Covers time-varying electromagnetic control relevant to radar waveform manipulation, sensing, and harmonic processing.	Primarily organized around space–time-coding principles and electromagnetic functionalities rather than metasurface positions in a radar architecture, radar-processing tasks, and quantitative system-level validation.
Saifullah et al. [28]	2022	Comprehensive review of electrical, optical, thermal, mechanical, and material-based tuning mechanisms, hardware implementations, programmable metasurfaces, RISs, and STAR-RISs.	Radar and sensing are included within a broad range of wireless, electromagnetic, and multifunctional applications.	Provides broad device- and application-level coverage, but radar functions, radar architectures, and experimental radar maturity are not used as its primary classification dimensions.

Table 1. *Cont.*

Representative Review	Publication Year	Principal Scope	Radar-Related Coverage	Scope Boundary Relative to the Present Review
Abdelraouf et al. [29]	2022	Active materials, tuning mechanisms, metasurface-design methodologies, machine-learning-assisted design, and application-oriented development of tunable metasurfaces.	Includes general sensing, imaging, beam control, and dynamically tunable electromagnetic and photonic devices.	Mainly material-, design-, and nanophotonics-oriented, with limited emphasis on microwave radar architectures, radar signal chains, and experimentally demonstrated radar-system metrics.
Liu et al. [30]	2023	Systematic categorization of reconfigurable metasurfaces based on five electromagnetic-wave dimensions and information-bit allocation, with detailed discussion of 1-bit and 2-bit elements.	Detection, sensing, imaging, communication, and computing are identified as potential application fields.	Establishes a general electromagnetic and information-based classification, but does not systematically map metasurfaces to radar transmitters, receivers, targets, RF processing stages, or experimental radar readiness levels.
Ullah et al. [31]	2024	Progression of conventional and modern RCS-reduction techniques, including platform shaping, radar-absorbing materials, scattering and absorption mechanisms, and active and passive metasurfaces.	Strongly focused on radar stealth, target signatures, conformal structures, polarization sensitivity, and RCS-reduction performance.	Does not provide an end-to-end treatment of reconfigurable metasurfaces used for radar transmission, reception, waveform generation, RF processing, computational imaging, localization, and multifunctional radar operation.
Shittu et al. [32]	2025	Physical principles and design methodologies of electromagnetic metamaterials for RCS reduction, including absorption, diffusion, polarization conversion, and scattering-cancellation mechanisms.	Provides detailed coverage of metamaterial-enabled target-side scattering suppression and stealth applications.	Primarily organized around RCS-reduction materials, mechanisms, and design procedures rather than complete metasurface-enabled radar architectures and quantitative comparisons of radar-system functions.
Present review	2026	Reconfigurable metasurfaces organized according to physical tuning mechanisms, controlled electromagnetic quantities, positions in the radar architecture, radar functions, and experimental maturity.	Covers target-side scattering control, transmit and receive apertures, waveform generation, RF preprocessing, computational imaging, sensing, localization, integrated sensing and communication, and radar countermeasures.	Establishes a radar-system-oriented framework connecting device reconfiguration, electromagnetic response, radar architecture, signal-processing function, experimental validation, and reported system-level performance.

Against the aforementioned research backdrop, this paper systematically reviews electromagnetic metasurfaces for radar wave modulation from a holistic radar-oriented perspective. First, we elaborate on the core physical mechanisms supporting electromagnetic wave control, including generalized scattering manipulation, digital and information metasurfaces, and time-varying and nonlinear theoretical frameworks, as well as polarization and geometric phase regulation. On this foundation, we further summarize mainstream metasurface solutions for RCS suppression and survey their applications in programmable beam scanning, synthetic aperture radar, and near-field imaging. Subsequently, we explore radar architectures built upon metasurfaces, such as time-domain modulated radar, computational radar, compressive sensing radar, MIMO radar, and ISAC platforms. Lastly, we investigate emerging application directions including radar stealth, deceptive jamming, LPI radar, artificial-intelligence-empowered cognitive radar, and multi-modal sensing. Finally, we provide an in-depth analysis of prevailing engineering obstacles and prospective research trends. Figure 1 illustrates the overall organizational framework of this review. Table 2 establishes a systematic taxonomy of metasurface-based aperture technologies for radar deployment.

Table 2. Taxonomy of metasurface-related aperture technologies for radar applications.

Technology	Core Feature	Typical Implementation	Radar Relevance	Key Distinction
Passive metasurface [15,33,34]	Fixed electromagnetic response after fabrication	Patterned passive unit cells, impedance surfaces, and geometric-phase elements	Fixed RCS reduction, beam shaping, polarization conversion, and absorber design	No real-time reconfiguration
Programmable metasurface [35,36]	Software-controlled electromagnetic response	PIN diodes, varactors, MEMS switches, tunable materials, and FPGA-based control circuits	Dynamic beam steering, adaptive scattering, and programmable RCS reduction	The aperture response can be updated electronically
Coding metasurface [20,21]	Discrete phase and/or amplitude states represented by digital codes	1-bit, 2-bit, or multi-bit unit cells arranged as spatial coding matrices	Programmable scattering, diffuse RCS reduction, and beam reconfiguration	Emphasizes the digital coding representation of the aperture
Information metasurface [35,37]	Joint manipulation of electromagnetic fields and digital information	Programmable coding surfaces integrated with real-time control and information-processing modules	Waveform manipulation, harmonic control, intelligent scattering, and integrated sensing and communication	Connects electromagnetic responses with information acquisition and processing operations
RIS [38–40]	Reconfigurable control of the wireless propagation environment	Passive or semi-passive reflecting elements with electronically controllable phase states	Radar-assisted communication, localization, environmental sensing, and ISAC scenarios	Usually channel-oriented rather than radar-front-end-oriented
Reflectarray [1,36]	Reflective aperture with spatial phase compensation	Patch or printed elements illuminated by a feed antenna	High-gain beamforming and low-profile radar apertures	An antenna-type reflector employing feed illumination

Table 2. *Cont.*

Technology	Core Feature	Typical Implementation	Radar Relevance	Key Distinction
Transmitarray [36,41]	Transmission-type aperture providing spatial phase control	Multilayer transmissive unit cells or electronically controlled phase-shifting elements	Lens-like beam shaping, beam steering, and low-sidelobe radiation control	Controls transmitted rather than reflected electromagnetic waves
Dynamic metasurface antenna [42–44]	Waveguide-fed and electronically tunable radiating aperture	Tunable metamaterial radiators coupled to guided waves	Computational imaging, synthetic-aperture radar, and compressive-sensing radar	Functions as a radiating aperture rather than an externally illuminated scattering surface
Leaky-wave aperture [42,44]	Guided-wave structure with controlled radiation leakage	Leaky-wave antennas, metamaterial waveguides, or frequency-diverse guided-wave apertures	Frequency scanning, computational imaging, and low-complexity radar apertures	Beam direction is generally frequency-dependent
Space–time-coding metasurface [45–47]	Joint spatial and temporal modulation of unit-cell states	Time-sequenced programmable elements controlled using periodic or coded modulation sequences	Harmonic beam steering, waveform generation, Doppler manipulation, low-probability-of-intercept operation, and radar deception [48,49]	Controls both the angular and spectral properties of scattering or radiation
Conventional phased array [1,2]	Element-level RF phase and amplitude control	Transmit/receive modules, phase shifters, RF chains, power amplifiers, and calibration networks	Mature high-performance radar architecture supporting agile beam steering and multifunction operation	Provides high performance but generally entails high size, weight, power consumption, cost, and thermal burden

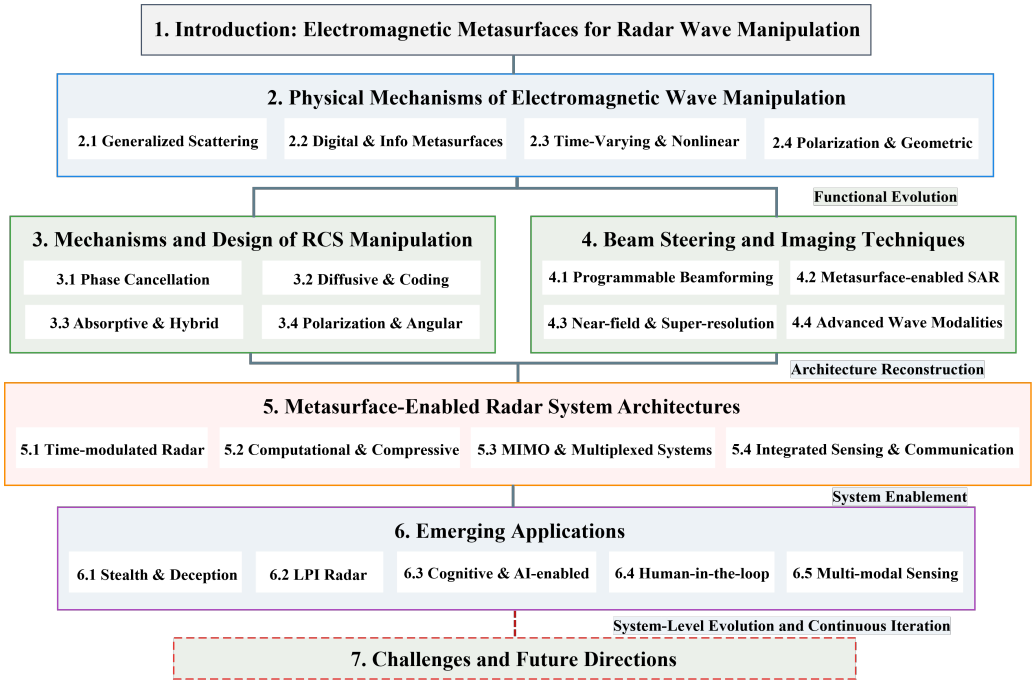


Figure 1. Electromagnetic metasurfaces for radar wave control: a panoramic framework for the radar-system-oriented review.

The categories in Table 2 are defined along several different dimensions and are therefore not strictly mutually exclusive. "Programmable metasurface" describes reconfigurability, whereas "reflectarray", "transmitarray", and "dynamic metasurface antenna" primarily describe aperture topology and excitation mechanism. "RIS" usually describes the system-level role of a surface in controlling an externally established propagation channel.

An externally illuminated programmable surface receives its incident field from a spatially separated transmitter and modifies the reflected or transmitted field. An RIS is commonly an externally illuminated surface deployed between a transmitter and a receiver to reconfigure the propagation channel; in sensing applications, it may redirect illumination or echoes but is not necessarily part of the radar transceiver. A reflectarray is a feed-illuminated reflective antenna that imposes a spatial phase distribution to form a radiated beam, whereas a transmitarray performs an analogous function in transmission. A dynamic metasurface antenna is instead a guided-wave-fed radiating aperture in which tunable metamaterial elements couple energy from an internal feed structure into free space.

Consequently, a programmable reflectarray may also be described as an RIS when it is used for channel control, and an information metasurface may be implemented using a reflective, transmissive, or guided-wave-fed topology. The terms should therefore be assigned according to excitation topology, radiating or scattering role, system position, and reconfigurability rather than treated as exclusive material classes.

Against this research backdrop, the core novelty of this survey lies in establishing systematic links among electromagnetic manipulation mechanisms, radar-specific functional designs, and practical deployment limitations. Instead of merely regarding metasurfaces as isolated electromagnetic structures, this review analyzes them as promising programmable aperture modules for next-generation radar architectures. This holistic structural framework allows readers to fully grasp not only the diverse radar functionalities that metasurfaces can deliver but also the critical engineering bottlenecks that need to be addressed prior to field deployment in real radar equipment.

2. Physical Mechanisms of Electromagnetic Wave Control

The unique radar wave manipulation capacity of electromagnetic metasurfaces fundamentally stems from the artificial reconfiguration of electromagnetic boundary conditions on two-dimensional interfaces at deep-subwavelength scales. Different from conventional bulk electromagnetic devices that accumulate phase along wave propagation paths, metasurfaces realize abrupt reshaping of electromagnetic phase, amplitude, polarization, and spectral responses at the interface via elaborate design on the spatial distribution of equivalent surface impedance or electric/magnetic surface polarizations [17,18,50]. This interface-dominated modulation paradigm shifts wave control from bulk propagation mechanisms to local scattering effects, enabling high-dimensional, multi-degree-of-freedom electromagnetic modulation while retaining an ultra-thin device profile.

From the perspective of technical evolution, the electromagnetic modulation mechanisms of metasurfaces have followed a continuous evolutionary progression: starting from static phase gradient design, advancing to discrete digital coding metasurfaces, and extending further to spatiotemporal modulation and polarization tuning [20,23,51]. This developmental trajectory marks a fundamental paradigm transition from a "structure-parameter-defined" modulation mode to an "information-and-spacetime co-governed" mode. Figure 2 illustrates a unified theoretical framework summarizing all metasurface electromagnetic modulation mechanisms. This section systematically elaborates on their core physical principles as well as their practical radar application potential across four categories: generalized scattering engineering, digital and information metasurfaces, time-varying nonlinear modulation, and polarization/geometric phase manipulation.

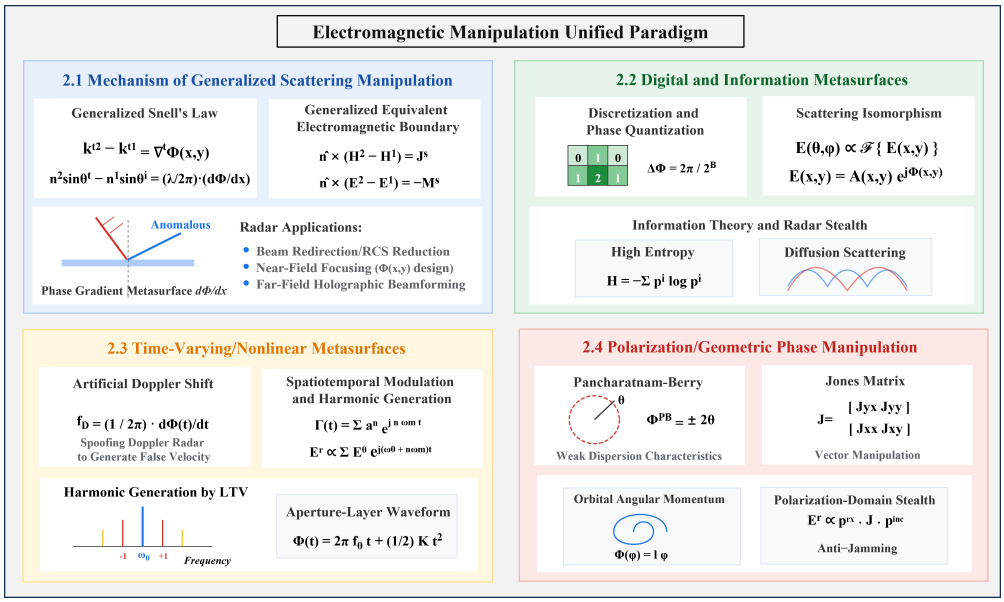


Figure 2. Unified framework of electromagnetic control mechanisms for metasurfaces. In the generalized scattering mechanism, anomalous beam deflection is induced by the transverse phase gradient of the metasurface, resulting in a reflected angle different from the specular reflection direction.

2.1. Generalized Scattering Engineering

In classical electromagnetism, the reflection and refraction of electromagnetic waves at uniform planar interfaces obey Snell's law, which is fundamentally governed by the conservation of tangential wavevector components at the boundary [52]. Nevertheless, the introduction of spatially varying phase discontinuities along the interface generalizes this conventional conservation principle, yielding the generalized Snell's law [15,53]. Its mathematical formulation is expressed as follows:

$$k_t^2 - k_t^1 = \nabla_t \Phi(x, y) \tag{1}$$

where $\mathbf{k}_t^1$ and $\mathbf{k}_t^2$ denote the tangential wavevector components of incident and outgoing electromagnetic waves, respectively. The operator ∇_t represents the transverse gradient along the metasurface plane, and $\Phi(x, y)$ is the spatially varying phase discontinuity introduced by the metasurface; $\nabla_t \Phi(x, y)$ denotes the interfacial phase gradient, corresponding to an additional transverse momentum term. This relation indicates that by designing a non-uniform phase distribution at the interface, the propagation direction of the incident wave can be directly manipulated, enabling anomalous reflection and anomalous refraction. In the one-dimensional case, this relation can be further expressed as follows:

$$n_2 \sin\theta_t - n_1 \sin\theta_i = \frac{\lambda}{2\pi} \frac{d\Phi}{dx} \tag{2}$$

where n_1 and n_2 are the refractive indices of the incident and transmission media, respectively; θ_i and θ_t denote the incident and transmitted angles measured with respect to the surface normal; λ is the free-space wavelength; and $d\Phi/dx$ is the phase gradient along the x-direction. For anomalous reflection in the same medium, a similar relation can be written by replacing the transmitted angle with the reflected angle θ_r.

From the perspective of boundary conditions, a metasurface can be equivalently represented as introducing electric and magnetic surface current sources at the interface, which satisfy the generalized electromagnetic boundary conditions [54]:

$$\hat{n} \times (\mathbf{H}_2 - \mathbf{H}_1) = \mathbf{J}^s, \quad \hat{n} \times (\mathbf{E}_2 - \mathbf{E}_1) = -\mathbf{M}^s \tag{3}$$

where $\hat{\mathbf{n}}$ is the unit normal vector pointing from medium 1 to medium 2; $\mathbf{E}_1$, $\mathbf{E}_2$, $\mathbf{H}_1$, and $\mathbf{H}_2$ are the total electric and magnetic fields on the two sides of the metasurface; $\mathbf{J}_s$ and $\mathbf{M}_s$ represent the equivalent electric and magnetic surface current densities, respectively. These equivalent surface currents describe the discontinuities of the tangential electromagnetic fields induced by the engineered metasurface.

Such equivalent surface sources are governed by the geometric profiles and material parameters of subwavelength scattering units and can be further translated into the spatial profile of equivalent surface impedance or polarization responses, which enables wavefront reconstruction at the meta-interface [33].

For radar application scenarios, the core value of this physical mechanism lies in that beam regulation and scattering manipulation can be directly implemented on an ultra-thin planar interface, eliminating the demand for phase accumulation along propagation paths that traditional reflectors and bulk lenses rely on. For example, when a linear phase gradient $\Phi(x) = k_x \sin\theta_r$ is patterned on the target surface, the dominant reflected scattering direction will deviate from the specular reflection direction. Reflected electromagnetic energy is thereby redirected toward directions outside radar detection coverage, realizing RCS suppression via beam redirection [55]. Since this modulation principle operates without dissipating electromagnetic energy, it exhibits advantages for wideband and low-loss working conditions.

In addition, when the phase profile is extended to a two-dimensional nonlinear function, metasurfaces are capable of sophisticated wavefront shaping. For instance, by elaborating a focusing phase distribution,

$$\Phi(x, y) = -k(\sqrt{(x - x_0)^2 + (y - y_0)^2 + f^2} - f) \tag{4}$$

metasurfaces can focus electromagnetic beams at a predefined spatial position, which further enables near-field imaging and high-resolution target sensing [56]. Meanwhile, holographic phase design allows the synthesis of arbitrary electromagnetic field distributions to generate multi-beam radiation and construct complex radiation patterns [57].

Although phase-gradient metasurfaces deliver a straightforward physical interpretation and abundant design freedom, their practical performance is frequently restricted by chromatic dispersion, angular sensitivity, and finite phase quantization discretization. Such drawbacks grow far more severe under broadband and large-aperture radar operating conditions, where beam squint, gain ripples, and wavefront distortion are inevitable [58,59]. Table 3 presents a detailed comparison of the associated engineering bottlenecks, and these challenges will be further elaborated in Section 7.

Table 3. Mechanism-level comparison of metasurface-enabled radar wave-manipulation approaches.

Approach	Typical Frequency Band	Bandwidth	Reconfigurability	Loss/Efficiency Issue	Power-Handling Consideration	Representative Radar Applications
Phase-gradient metasurface [15,19,33,54]	Microwave/millimeter-wave	Narrow to moderate; often dispersion-limited	Mostly static; tunable versions possible	Low loss in passive designs, but phase dispersion and angular sensitivity exist	Relatively high for passive structures	Beam steering, anomalous reflection, and RCS redirection
Digital/coding metasurface [20,21,35]	Microwave/millimeter-wave	Moderate; depends on unit-cell design and coding states	Digitally programmable with discrete states	Quantization error, insertion loss, and element mismatch	Limited by active-device breakdown and nonlinear response	Programmable scattering, diffuse RCS reduction, and beam reconfiguration

Table 3. *Cont.*

Approach	Typical Frequency Band	Bandwidth	Reconfigurability	Loss/Efficiency Issue	Power-Handling Consideration	Representative Radar Applications
Absorptive metasurface [60–62]	Microwave to terahertz depending on materials	Narrow to broadband depending on structure	Mostly passive; tunable absorption possible	Intentional energy dissipation and thermal load	Strongly limited by heat dissipation and material reliability	RCS reduction, stealth, and absorber-backed aperture design
Hybrid absorptive–diffusive metasurface [63–65]	Mainly microwave/millimeter-wave	Moderate to broadband	Static or semi-reconfigurable	Combines absorption loss and scattering redistribution	Thermal management and structural reliability are important	Multistatic RCS reduction and broadband stealth
Polarization-control metasurface [34,66–68]	Microwave/ millimeter-wave/ optical	Often broadband with geometric phase but polarization-dependent	Static or switchable	Conversion efficiency and polarization mismatch affect performance	Usually moderate; depends on active or passive implementation	Polarimetric control, anti-jamming, and polarization-domain stealth
Time-varying/space–time metasurface [45–47]	Mainly micro/millimeter-wave in current demonstrations	Determined by modulation speed and unit-cell bandwidth	Highly reconfigurable in space and time	Modulation loss, harmonic leakage, and spectral impurity	Limited by active components under high-power radar signals	Doppler manipulation, waveform generation, and LPI/deception, harmonic beam control
Dynamic metasurface antenna [42–44]	Microwave/millimeter-wave	Moderate; depends on feed and radiating-element design	Pattern-programmable	Aperture efficiency, feed loss, and mode correlation	Limited by element design and control electronics	Computational imaging, SAR, MIMO radar, and compressive sensing

2.2. Digital and Information Metasurfaces

To overcome the limitations of continuous phase designs in terms of complexity and reconfigurability, digital coding metasurfaces discretize the electromagnetic response and introduce concepts from information theory and digital signal processing, thereby achieving an "information-theoretic description" of the electromagnetic aperture [24]. In this framework, each metasurface unit cell assumes only a finite number of discrete states. For example, in n-bit coding, the set of phase states can be expressed as follows:

$$\Phi_q \in \left\{0, \frac{2\pi}{2^n}, \ldots, \frac{2\pi(2^n-1)}{2^n}\right\} \tag{5}$$

where n denotes the number of quantization bits, and $q = 0, 1, \ldots, 2^n - 1$ denotes the coding state index.

Consequently, the full metasurface aperture can be abstracted into a discrete digital coding matrix, whose spatial arrangement directly governs the electromagnetic scattering characteristics. This mathematical representation converts metasurfaces from analog devices dependent on continuous geometric modulation into electromagnetic aperture platforms capable of fast reconfiguration via digital control.

Under the far-field approximation, the scattering behavior of a coding metasurface exhibits a close correspondence with the spatial Fourier transform of its aperture complex weighting function [69,70]. Let the aperture complex weighting function be as follows:

$$E(x, y) = A(x, y)e^{j\Phi(x,y)} \tag{6}$$

Then, the far-field scattering can be expressed as follows:

$$E(\theta, \phi) \propto \mathcal{F}\{E(x, y)\} \tag{7}$$

This mathematical relation uncovers a core physical nature, namely the isomorphism between the spatial coding layout of metasurface units and the angular-domain scattering pattern. In other words, the metasurface design problem can be converted into a far-field spectral shaping task, where target scattering patterns can be realized by tuning the digital coding matrix [71]. This theoretical viewpoint unifies electromagnetic scattering engineering and digital signal processing from the perspective of mathematical formalism, which greatly cuts down design complexity and enhances the flexibility of electromagnetic manipulation.

In radar scattering control, information theory further provides an important tool for quantifying the coding structure [72]. For example, coding entropy can be defined as follows:

$$H = -\sum_{i=1}^{N} p_i \log_2 p_i \tag{8}$$

where p_i denotes the probability distribution of each independent coding unit state. High-entropy metasurface coding exhibits higher spatial randomness, which suppresses specular reflection and disperses electromagnetic energy across a broader angular range to realize RCS suppression via diffusive random scattering. Compared with conventional loss-absorption stealth schemes, this mechanism achieves radar stealth via electromagnetic energy redistribution instead of energy dissipation, thus presenting potential advantages in thermal management and wideband compatibility [63].

Nevertheless, the practical performance of digital coding metasurfaces remains limited by various non-ideal factors. Phase quantization errors resulting from a finite number of bits introduce wavefront distortion in the form of "phase noise" [73], with a quantization step size of

$$\Delta\Phi = \frac{2\pi}{2^n} \tag{9}$$

Furthermore, electromagnetic mutual coupling between unit cells within dense metasurface arrays invalidates the ideal assumption of independent unit coding, and the resultant electromagnetic response deviates from the pre-designed values. With an enlarged aperture size, the control system suffers from drastically increased complexity; technical challenges including biasing network design, synchronous control, and real-time reconfigurability emerge as major system bottlenecks. To address the above electromagnetic and hardware limitations, researchers have further shifted their focus to time-varying and space–time programmable metasurfaces.

2.3. Time-Varying and Nonlinear Metasurfaces

Conventional metasurfaces generally work under linear time-invariant (LTI) conditions, whose output spectra match the input spectra exactly. Once temporal modulation is applied to render metasurface parameters time-dependent, the metasurface system becomes a linear time-varying (LTV) system and allows energy redistribution across the frequency domain [45]. The reflection coefficient can be formulated as follows:

$$\Gamma(t) = \sum a_n e^{jn\omega_m t} \tag{10}$$

For an incident single-frequency signal $E_i = E_0 e^{j\omega_0 t}$, the reflected signal will contain multiple harmonic components:

$$E_r \propto \sum a_n E_0 e^{j(\omega_0 + n\omega_m)t} \tag{11}$$

This indicates that time-varying metasurfaces can achieve frequency conversion and spectral manipulation at the interface layer.

When temporal modulation is further extended to joint space–time modulation, the system exhibits more abundant frequency–angle coupling features [35]. For example, by tailoring the space–time phase distribution $\Phi(x, t)$, we can allocate separate frequency components to independent radiation directions and thus realize parallel manipulation of multi-frequency multi-beam radiation. This unique functionality offers an innovative aperture multiplexing scheme for radar systems, which allows one single physical aperture to execute multiple tasks simultaneously [21].

The introduction of temporal degrees of freedom marks a critical evolution of metasurface technology, shifting its working paradigm from static spatial field manipulation to dynamic electromagnetic regulation. Relevant engineering implementations and radar-oriented functions empowered by time-varying metasurfaces—including Doppler modulation, waveform synthesis, and multifunctional radar operation—will be elaborated in subsequent sections.

2.4. Polarization and Geometric Phase Control

Electromagnetic waves are vector fields, and their polarization states play a critical role in radar detection and target identification. Equipped with anisotropic scatterers, metasurfaces allow precise modulation of electric field vectors, whose polarization responses can be characterized via the Jones matrix [74]:

$$J = \begin{bmatrix} J_{xx} & J_{xy} \\ J_{yx} & J_{yy} \end{bmatrix} \tag{12}$$

Tailoring the spatial layout of matrix elements enables the implementation of polarization rotation, polarization conversion, and cross-polarization manipulation [75].

Cutting-edge research has pushed polarization manipulation forward to versatile transmissive metadevices. For instance, 3D-printed transmissive metasurfaces realize wavefront shaping based on polarization division, which integrates multiple independent electromagnetic functions within a single compact aperture [76].

Building upon polarization modulation theories, the geometric phase (Pancharatnam–Berry phase, PB phase) acts as a powerful phase regulation strategy for metasurfaces. For an ideal anisotropic unit cell, its physical rotation angle θ introduces an extra geometric phase shift:

$$\Phi_{PB} = \pm 2\theta \tag{13}$$

Governed purely by geometric rotation, the PB phase suffers minimal dispersion and thus exhibits advantages for broadband radar systems [77]. By arranging the spatial distribution of unit rotation angles, intricate wavefronts such as orbital angular momentum (OAM) beams can be generated, following the phase relation below:

$$\Phi(\phi) = l\phi \tag{14}$$

This property further facilitates multi-modal electromagnetic wave regulation and electromagnetic information multiplexing [78].

Within radar architectures, polarization modulation delivers an extra degree of freedom separate from conventional amplitude-phase tuning. As an illustrative example, elaborately designed polarization converters can create polarization mismatch between target echoes and receiving channels to weaken the magnitude of effective received signals. The received electric field is formulated as follows:

$$E_r \propto \mathbf{p}_{rx} \cdot J \cdot \mathbf{p}_{inc} \tag{15}$$

Modulating the Jones matrix J minimizes this polarization projection, which endows the system with polarization-domain stealth and anti-interference performance [66].

Nevertheless, the performance of such polarization-based schemes strongly relies on the radar's polarization hardware framework. If the radar system supports polarization diversity, the echo suppression capacity offered merely by polarization conversion will deteriorate drastically. In addition, PB phase generation demands strict polarization incidence conditions, which creates severe compatibility barriers when cooperating with conventional linearly polarized radar systems [79].

2.5. Section Summary

In summary, the regulation principles of electromagnetic metasurfaces can be unified into four core dimensions: phase, digital information, time, and polarization. Phase gradients realize wavefront shaping; digital coding achieves control over angular-domain energy distribution; spatiotemporal modulation injects extra degrees of freedom in both frequency and Doppler domains; polarization coupled with geometric phases extends the manipulation capacity of vector electromagnetic waves [36,80,81]. Collectively, these multi-dimensional regulation rules push metasurface development from conventional passive electromagnetic interfaces to electronically reconfigurable or software-controlled apertures and establish the physical underpinnings for radar scattering manipulation, beam steering, and system architecture innovations that follow. To facilitate intuitive comparisons among diverse radar implementations empowered by metasurfaces, Table 3 provides a mechanism-level overview of the principal metasurface approaches, whereas a study-specific quantitative comparison of experimentally demonstrated radar systems and subsystems is provided in Section 5.6.

3. Radar Cross Section Engineering

RCS reduction via electromagnetic metasurfaces represents one of the earliest and most practically oriented research branches of metasurface technology, which directly targets the actual demands of radar systems. Unlike conventional stealth technologies that rely on profile shaping and radar absorbing materials (RAMs), metasurfaces can reconstruct electromagnetic boundary conditions at subwavelength scales on demand, turning the whole scattering behavior into a customizable design variable. This property enables multi-dimensional manipulation of scattering amplitude, phase, polarization, and angular distribution. The paradigm shift from "structural stealth" to "scattering engineering" redefines RCS suppression: instead of merely optimizing material composition and geometric contours, researchers can regulate wavefronts and encoded information, which provides a potential approach for radar countermeasures under complex electromagnetic environments [14,20,26]. Based on the generalized scattering engineering, digital coding, and time-modulation theories elaborated in Section 2, this chapter systematically reviews four mainstream metasurface-enabled RCS suppression strategies, namely phase interference, spatial diffusion, energy dissipation, and polarization/angular modulation and analyzes their respective performance characteristics. Figure 3 depicts typical metasurface schemes dedicated to RCS reduction.

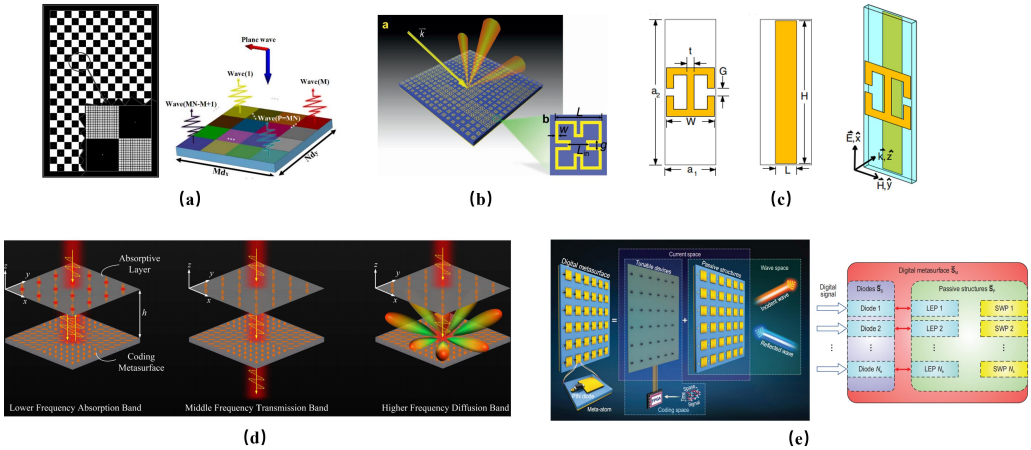


Figure 3. Representative metasurface structures and supporting models for radar-cross-section control. (**a**) Conventional checkerboard and optimized multielement phase-cancellation arrangements, reproduced from Ref. [82]. (**b**) Multi-bit coding metasurface for broadband diffuse scattering, reproduced from Ref. [83]. (**c**) Perfect metamaterial absorber based on impedance matching and dissipative loss, reproduced from Ref. [60]. (**d**) Hybrid absorptive–diffusive frequency-selective structure, reproduced from Ref. [65]. (**e**) Macroscopic and statistical electromagnetic-information models of a digital coding metasurface, reproduced from Ref. [84].

3.1. Phase Cancellation Mechanisms

The phase cancellation mechanism ranks among the earliest strategies proposed for metasurface-enabled RCS mitigation and features an extremely straightforward physical interpretation. This method relies on coherent interference within the generalized scattering manipulation framework. Arranging multiple scattering zones on the target surface with nearly identical reflection magnitudes yet reversed phases allows destructive interference to form along radar sightlines, which suppresses specular backscattering. We consider two kinds of equivalent scatterers whose reflection coefficients are formulated as

$$\Gamma_1 = A_1 e^{j\phi_1}, \quad \Gamma_2 = A_2 e^{j\phi_2} \tag{16}$$

the resultant scattered field in the observation direction can be expressed as

$$E_s \propto A_1 e^{j\phi_1} + A_2 e^{j\phi_2} \tag{17}$$

When the two criteria $\phi_1 - \phi_2 \approx \pi$ and $A_1 \approx A_2$ are satisfied, strong field cancellation occurs along the observation direction and yields evident RCS mitigation [55,85,86]. Guided by this interference principle, checkerboard metasurfaces stand as the most representative implementation structure. Periodic interleaving of artificial magnetic conductor (AMC) and impedance unit cells enables the metasurface to approximately meet the anti-phase condition around the target operating frequency and thus suppress backscattering efficiently. Figure 3a juxtaposes a conventional checkerboard configuration with an optimized multielement phase-cancellation arrangement. Both schemes rely on destructive interference in the specular direction, whereas the optimized multielement design broadens the RCS-reduction bandwidth by introducing multiple engineered reflection-phase responses.

For radar practical deployment, phase-canceling metasurfaces exhibit advantages including simple geometry and minimal dissipative loss. Nevertheless, their practical performance is constrained by three inherent drawbacks: narrow working bandwidth, high angular sensitivity, and the fact that scattered energy is merely spatially redistributed instead of fully suppressed [67,82,87,88]. Accordingly, their stealth capability will deteriorate severely under multistatic and distributed radar working conditions.

3.2. Diffusive and Coding-Based Scattering

To address the bandwidth and angular stability drawbacks of phase cancellation schemes, researchers have put forward and vigorously advanced diffuse scattering techniques based on digital coding. Such strategies discretize continuous phase responses into a limited number of phase states. By adopting pseudorandom or optimized spatial coding sequences, they decohere the aperture's spatial spectrum and thus attenuate intense deterministic specular echoes. From far-field diffraction theory, the angular scattering profile of a metasurface approximates the spatial Fourier transform of its complex reflection coefficient distribution:

$$E(\theta, \phi) \propto \sum_{m,n} A_{m,n} e^{j\phi_{m,n}} e^{-j\mathbf{k}\cdot\mathbf{r}_{m,n}} \tag{18}$$

If the phase layout carries sufficient randomness, scattered waves cease intense coherent superposition across the angular range and display nearly homogeneous diffuse scattering behavior, which drastically suppresses peak RCS values [83,89,90].

To quantify the randomness of coding metasurfaces and its influence on scattering signatures, information entropy is adopted as a core quantitative evaluation indicator. For a coding metasurface equipped with N discrete phase states, Shannon entropy is defined as

$$H = -\sum_{i=1}^{N} p_i \log_2 p_i \tag{19}$$

where p_i denotes the probability of occurrence for each coding state. High-entropy coding schemes generally yield more homogeneous angular energy distribution, which delivers suppressed peak RCS levels [72,91,92]. Based on this entropy theory, global optimization of coding layouts can be implemented via intelligent optimization algorithms including genetic algorithms and particle swarm optimization, with optimization targets of minimizing peak scattering magnitude or reshaping angular energy distribution [73,93,94]. As illustrated in Figure 3b, a multi-bit coding metasurface redistributes the scattered power over multiple spatial directions, thereby reducing the peak scattering intensity in the specular direction. Figure 3e presents a macroscopic and statistical modeling framework that connects digital coding states, equivalent surface currents, and radiated fields. It should be regarded as a supporting analytical framework for coding-based scattering control rather than as an independent RCS-reduction mechanism.

Compared with phase cancellation technology, coded diffuse scattering realizes stable peak RCS attenuation within a broader angular coverage range. Nevertheless, its overall performance remains vulnerable to phase quantization errors, frequency dispersion effects, and predictable coding sequences [21,35,84]. To sustain long-term electromagnetic countermeasures against cognitive and multistatic radar systems, static coding schemes require hybridization with absorptive structures or dynamic reconfiguration modules.

3.3. Absorptive and Hybrid Designs

Although diffuse scattering effectively suppresses specular reflection peaks, it merely serves as an energy reallocation scheme. Under ideal lossless assumptions, the overall scattered power is conserved entirely. In multistatic and distributed radar architectures, such rerouted scattering energy can still be captured by auxiliary receiving nodes. To achieve substantial reduction of total scattering cross-section, absorptive mechanisms are indispensable core solutions. Absorptive metasurfaces are designed to tune surface equivalent impedance for near-perfect matching with free-space impedance within the target operating band,

which weakens reflected waves and boosts electromagnetic energy loss. The reflection coefficient is formulated as follows:

$$\Gamma = \frac{Z_s - Z_0}{Z_s + Z_0} \tag{20}$$

When $Z_s \approx Z_0$, the reflected field magnitude is drastically attenuated. For metal-backed substrates, absorptivity follows the approximation $A = 1 - |\Gamma|^2$, which reveals that minimal reflection yields superior wave absorption performance [60–62].

However, fully absorptive metasurface architectures generally rely on stacked multilayers or high-loss dielectrics, bringing non-negligible penalties in device thickness, weight, and thermal control. To reconcile wave-absorbing performance with practical engineering realizability, hybrid metasurfaces integrating energy absorption and coded diffuse scattering have been proposed in recent years. Their equivalent reflection weight function is formulated as follows:

$$w(x, y) = A(x, y)e^{j\phi(x,y)} \tag{21}$$

where the amplitude component $A(x, y)$ governs the absorption depth, while the phase term $\phi(x, y)$ manipulates the angular distribution of scattered power. This dual synergistic regulation simultaneously suppresses total scattered energy and directional scattering lobes, which yields outstanding multi-scenario stealth capacity under complex electromagnetic environments [64,65,95,96]. Figure 3c illustrates a perfect metamaterial absorber based on impedance matching and dissipative loss. The hybrid absorptive–diffusive frequency-selective configuration shown in Figure 3d combines frequency-selective absorption with angular redistribution of the residual scattered energy.

From a system-level perspective, though lossy absorption improves stealth performance against multistatic radar systems, it also introduces three prominent engineering drawbacks: thermal buildup from dissipated energy that amplifies infrared radiation signatures, bulky multilayers hindering seamless platform integration, and long-term durability degradation of functional materials and components. Accordingly, absorptive and hybrid metasurface schemes require joint optimization alongside platform thermal design and multispectral stealth specifications in real-world deployment.

3.4. Polarization and Angular Control

Beyond amplitude and phase modulation, polarization introduces an extra critical degree of freedom for RCS manipulation. Radar systems transmit and receive electromagnetic waves via dedicated polarization channels; accordingly, polarization conversion cuts down the effective polarization inner product of target echoes at receiving ports. The polarization response of metasurfaces is fully characterized by the Jones matrix:

$$\mathbf{E}_r = J\mathbf{E}_i \tag{22}$$

The corresponding received field amplitude follows the following relation:

$$E_{rec} \propto \mathbf{p}_r^T J \mathbf{p}_i \tag{23}$$

where $\mathbf{p}_i$ and $\mathbf{p}_r$ denote incident and receiving polarization vectors, respectively [34,75,97]. By integrating anisotropic meta-atoms that convert incident waves into orthogonal polarization states, we can drastically weaken the detection performance of single-polarization radar equipment.

Nevertheless, the suppression performance of polarization manipulation strongly depends on the radar's polarization hardware framework. If radar platforms support polarization diversity or full-polarimetric detection, the echo attenuation brought solely

by polarization conversion will decline markedly. For practical engineering deployment, polarization modulation is usually combined with diffuse scattering or wave-absorbing strategies to realize full-coverage RCS suppression [67,68,98].

In parallel, phase-gradient angular steering delivers a straightforward route to redirect scattered wave propagation directions. As elaborated in Section 2.1, metasurfaces engineered with transverse phase gradients deflect scattered power away from specular reflection paths. Such a scheme achieves remarkable monostatic RCS mitigation [15,53,99], yet the deflected scattered energy remains susceptible to capture by multistatic radar networks.

3.5. Section Summary

This chapter systematically summarizes core operating principles and technical characteristics of metasurface-based radar cross-section regulation under four distinct technical branches: phase cancellation, coded diffuse scattering, absorptive and composite architectures, as well as polarization and angular modulation. Phase cancellation delivers a simple, readily engineered solution to suppress specular backscattering, yet it suffers intrinsic limitations on operating bandwidth and angular stability. Coded diffusion strategies realize wide-angle RCS attenuation via spatial field decoherence and greatly strengthen adaptability in complicated electromagnetic environments. Absorptive and composite metasurfaces further cut total scattering cross-section from energy dissipation perspectives, which constitutes a vital technical route for multistatic radar countermeasures. Polarization and angular tuning expand the available degrees of freedom within scattering manipulation and supply essential tools for multi-dimensional joint stealth regulation. Figure 4 conducts a multi-dimensional horizontal comparison of all typical metasurface RCS suppression mechanisms. To conclude, metasurface scattering shaping technology has evolved from single-mechanism optimization to multi-mechanism fusion and system-level co-design. Its technical roadmap shifts from static passive layouts to reconfigurable, time-variant, and information-aware dynamic modulation, which establishes a solid theoretical foundation for future intelligent radar countermeasure systems and multi-spectrum stealth devices. Beyond pure backscatter reduction, the multi-dimensional manipulation of amplitude, phase, polarization, and angular wavefront distribution also underpins the synthesis of active electromagnetic apertures. Accordingly, radar functions empowered by metasurfaces expand beyond passive stealth scattering control to advanced beamforming, radar imaging, and integrated multifunctional electromagnetic apertures.

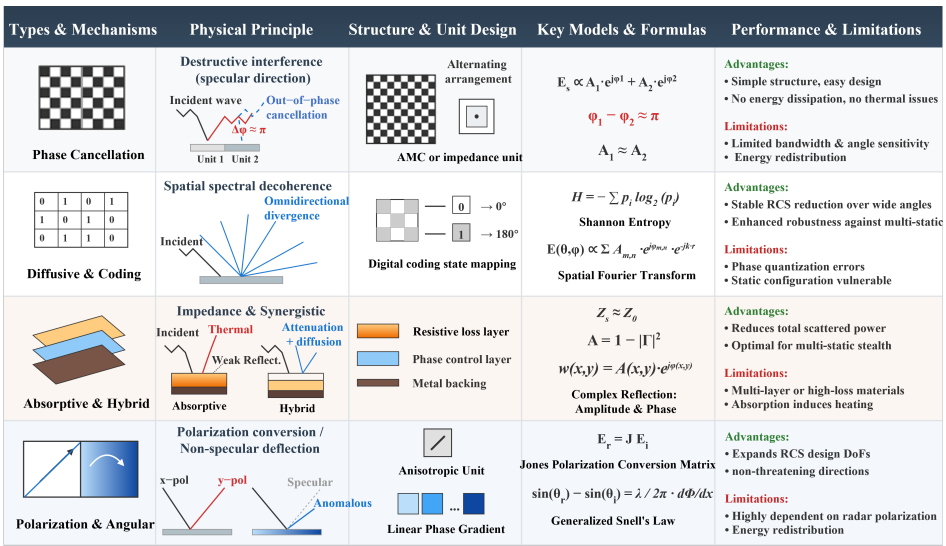


Figure 4. Four typical radar cross-section (RCS) control mechanisms based on electromagnetic metasurfaces: comparison of principles, structures, mathematical models, and system performance [55,82].

4. Beamforming and Imaging with Metasurfaces

By reconstructing subwavelength electromagnetic boundary conditions, electromagnetic metasurfaces facilitate a distinct paradigm shift in radar beamforming and imaging. Traditional radar systems rely on complex RF feeding networks and distributed phase-shifting chains, whereas metasurfaces enable a new implementation scheme based on programmable electromagnetic apertures. This advancement realizes direct wavefront synthesis at the physical aperture plane, which may offer a route toward reducing selected RF front-end components and associated system overhead, although system-level SWaP benefits have not yet been established through controlled comparative experiments. Based on the fundamental electromagnetic modulation mechanisms in Section 2 and diverse scattering engineering strategies in Section 3, this chapter systematically explores the functional roles and performance limitations of metasurfaces in radar systems from four aspects: programmable beam regulation, metasurface-assisted synthetic-aperture radar (SAR), near-field super-resolution imaging, and innovative electromagnetic wave modality manipulation. Figure 5 demonstrates typical metasurface-enabled beam control and imaging techniques.

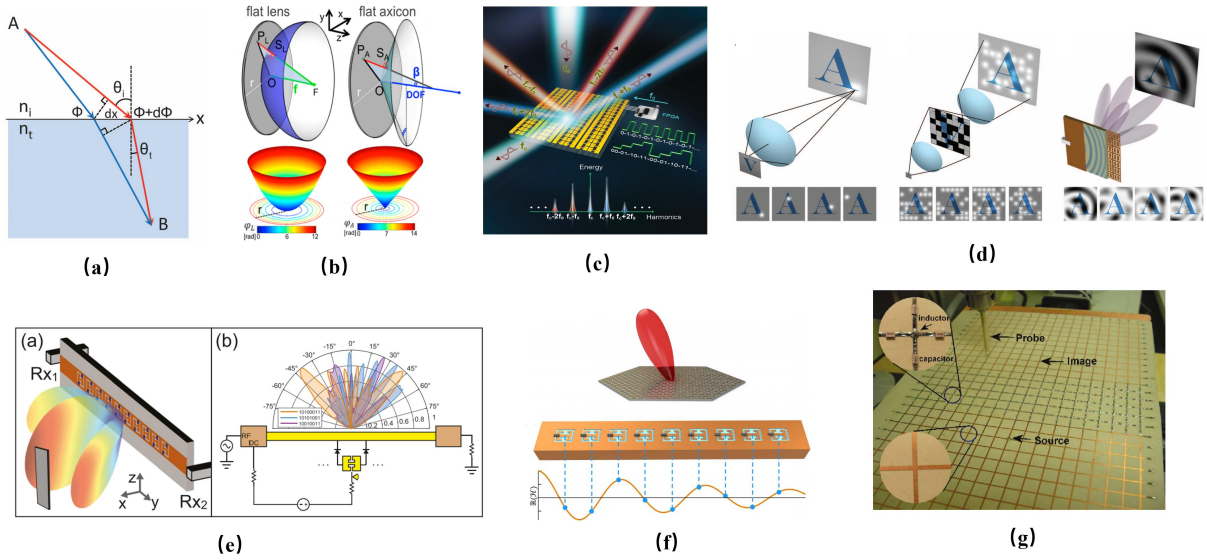


Figure 5. Representative wavefront-control and computational-imaging concepts relevant to metasurface-enabled radar. (**a**) Generalized laws of reflection and refraction based on an interfacial phase discontinuity, reproduced from Ref. [15]. (**b**) Ultra-thin planar lenses and axicons implemented using spatial phase distributions, reproduced from Ref. [56]. (**c**) Time-domain digital-coding metasurface for programmable harmonic and beam manipulation, reproduced from Ref. [35]. (**d**) Computational metamaterial-aperture imaging framework based on coded measurements and image reconstruction, reproduced from Ref. [42]. (**e**) Dynamic metamaterial aperture for compressive microwave imaging, reproduced from Ref. [43]. (**f**) Dynamic metasurface antenna concept for synthetic-aperture-radar imaging, reproduced from Ref. [100]. (**g**) Experimental configuration of a planar left-handed transmission-line lens used to demonstrate sub-diffraction near-field imaging, reproduced from Ref. [101].

4.1. Programmable Beamforming

In the far-field regime, the radiation behavior of a metasurface aperture can be mathematically mapped to the spatial Fourier transform of its complex reflection or transmission coefficient distribution. For a planar aperture located in the $z = 0$ plane, define the scalar complex aperture distribution as

$$A(x, y) = \alpha(x, y) \exp[j\phi(x, y)], \tag{24}$$

where $\alpha(x, y)$ is the dimensionless amplitude weighting, and $\phi(x, y)$ is the local aperture phase in radians. Under a homogeneous medium, narrowband excitation, scalar-aperture approximation, Fraunhofer observation, and negligible mutual coupling and element-pattern variation, the far-field pattern is proportional to

$$E(\theta, \varphi) \propto \iint_{\mathcal{A}} A(x, y) \exp\{-jk[x \sin\theta \cos\varphi + y \sin\theta \sin\varphi]\} \, \mathrm{d}x \, \mathrm{d}y, \tag{25}$$

where $k = 2\pi/\lambda$ is the free-space wavenumber in rad m^{-1}, λ is the wavelength in metres, θ and φ are the observation elevation and azimuth angles, and $\mathcal{A}$ denotes the physical aperture domain.

This Fourier mapping reveals that the beam steering direction is predominantly governed by the linear phase gradient profile, while the sidelobe level and beamwidth are co-determined by the aperture amplitude weighting and physical aperture size. A linearly distributed phase profile enables precise main-beam steering toward preset angular directions. Physically, such beam manipulation mechanism shares the same working essence as aperture-level phase synthesis in conventional phased arrays, whereas the implementation paradigm shifts from traditional RF phase-shifting networks to interface-native phase modulation [15,20,33,102].

The integration of digital coding and active components further upgrades static metasurface apertures to dynamically programmable electromagnetic systems. As elaborated in Section 2.2, programmable metasurfaces support discretized phase states with finite quantization levels. Real-time updating of the spatial coding matrix enables flexible beam scanning and radiation pattern reconfiguration without repetitive theoretical derivation. This information-programmed modulation allows a single physical aperture to switch among diverse operational tasks, such as adaptive beam shaping for radar searching and tracking, which substantially improves the overall system reconfigurability [21,35,90]. As illustrated in Figure 5c, time-domain digitally coded metasurfaces realize dynamic harmonic and beam regulation via programmable spatial modulation.

From a system-level perspective, metasurface-based beamformers exhibit compelling performance in terms of peak gain, sidelobe suppression, and angular scanning capability across microwave and millimeter-wave bands. Nevertheless, most existing designs adopt passive or quasi-passive architectures, where the radiation power fully relies on external feeding sources. This induces inherent trade-offs between aperture simplification and radiation efficiency in system link budget design. Furthermore, frequency dispersion of meta-atom responses leads to inevitable beam squinting under wideband operation. In addition, incident-angle sensitivity and phase quantization errors introduce wavefront distortion and sidelobe deterioration for large-scale aperture arrays. Collectively, these physical constraints define the performance limits of metasurface beamformers in wideband and wide-angle scanning applications.

4.2. Metasurface-Enabled SAR

Conventional synthetic-aperture radar forms a large effective aperture by coherently combining measurements acquired at different spatial positions along a platform trajectory. The resulting azimuth resolution is determined by the spatial phase history accumulated over the synthetic aperture rather than by the number of electronic states available at a fixed physical aperture.

In metasurface-enabled SAR, a dynamic metasurface antenna serves primarily as a reconfigurable transmitting or receiving aperture. It can modify the illumination pattern, steer the beam, generate frequency-diverse radiation modes, or provide several coded measurements at each platform position. These functions may reduce the complexity of

conventional feed and beamforming networks and can improve measurement diversity. However, switching the metasurface states at a fixed position does not, by itself, generate the spatial baseline required for conventional SAR. Physical platform motion, or an equivalent distributed or multichannel observation geometry, remains necessary to synthesize the along-track aperture.

Under a simplified broadside, monostatic, narrowband, far-field geometry, the cross-range resolution associated with a coherently processed synthetic aperture of length L_{sa} may be approximated as

$$\delta_{\mathrm{az}} \approx \frac{\lambda R_0}{2L_{\mathrm{sa}}}, \tag{26}$$

where λ is the operating wavelength, R_0 is the nominal slant range, and L_{sa} is the coherent synthetic-aperture length. The exact coefficient depends on the imaging geometry, antenna pattern, weighting, and processing convention. Metasurface reconfiguration changes the illumination and measurement operator, but it does not alter this fundamental requirement for spatially distributed coherent observations [43,103,104]. Figure 5f demonstrates the low-complexity beam scanning and imaging capabilities enabled by dynamic metasurface-based SAR antennas.

Furthermore, dynamic coded SAR systems impose stringent requirements on phase coherence and calibration precision. Since coherent superposition dominates the entire imaging procedure, trivial unit errors and temporal control delays will accumulate across large-scale aperture arrays, triggering severe degradation of focusing accuracy. Accordingly, system-level error modeling and calibration compensation techniques are indispensable guarantees for high-precision metasurface imaging performance.

4.3. Near-Field Focusing and Resolution-Enhancement Mechanisms

A metasurface can compensate for the propagation phase from different aperture positions to a prescribed focal point. When the field is composed primarily of propagating spatial frequency components, the focal spot remains governed by the effective numerical aperture, operating wavelength, propagation distance, aperture size, and illumination bandwidth. Such focusing can improve local field strength, signal-to-noise ratio, and imaging contrast, but it does not by itself constitute super-resolution beyond the diffraction limit [56,77,101].

Computational and coded-aperture systems acquire a set of diverse measurements and reconstruct the scene using an assumed forward model. When the scene contains a small number of isolated scatterers and the sensing matrix has sufficient diversity, sparse or parametric reconstruction may distinguish targets with separations smaller than the conventional matched-filter or Rayleigh resolution. This is a model-based resolution enhancement that relies on sparsity, adequate signal-to-noise ratio, accurate calibration, and low mutual coherence of the measurement matrix. It should not be interpreted as the general physical recovery of arbitrary subwavelength spatial frequency content.

Physical subwavelength imaging requires access to high-transverse-wavenumber components that are evanescent in free space. Near-field superlenses, hyperbolic structures, and related metamaterial or metasurface devices can enhance, transfer, or convert part of this evanescent spectrum into detectable signals. This mechanism is physically distinct from propagating-wave focusing and sparse reconstruction. Its performance is generally restricted to short working distances and is sensitive to material loss, dispersion, fabrication error, and bandwidth.

Leveraging this near-field focusing principle, metasurfaces have been extensively exploited in through-wall detection, security screening, and high-precision short-range structural sensing. The localized field enhancement effectively boosts echo amplitude under

fixed transmit power, yielding improved imaging contrast and detection sensitivity. When integrated with computational imaging and sparse reconstruction algorithms, metasurface platforms are capable of breaking conventional diffraction limits and realizing enhanced near-field imaging resolution. Figure 5d illustrates a universal computational imaging framework that formulates imaging as a matrix measurement and reconstruction problem; Figure 5e presents dynamic metamaterial apertures that implement compressed sensing imaging via multi-modal radiation diversity; Figure 5g demonstrates super-resolution imaging beyond the diffraction limit using left-handed material superlenses.

Nevertheless, metasurface near-field imaging exhibits inherent distance-dependent characteristics. High-quality focusing generally relies on prior target information or adaptive scanning compensation. Furthermore, the intrinsic near-field coverage constraint restricts its effective operating range, making such schemes well-suited for short-range high-precision detection but incompatible with long-range radar deployment.

4.4. Advanced Wave Modalities

Beyond standard plane waves and focused beams, metasurfaces support the generation and flexible regulation of diverse exotic electromagnetic wave modes, among which OAM vortex waves stand as the most representative category. OAM beams feature helical phase fronts, whose azimuthal phase profile follows the relation

$$E(\phi) \propto e^{jl\phi} \tag{27}$$

where l denotes the topological charge value. By patterning helical phase distributions or adopting rotation-modulated meta-cells governed by the Pancharatnam–Berry (PB) phase, compact planar metasurfaces can generate and dynamically switch OAM eigenmodes [78,105,106].

For radar detection tasks, OAM vortex beams supply an extra angular-domain modulation degree of freedom, which improves the capacity to distinguish targets and separate multiple scattering centers. Nevertheless, high-order OAM modes suffer severe far-field divergence in real propagation and scattering environments, which degrades energy utilization efficiency for long-distance radar detection. Meanwhile, finite-aperture truncation, multipath echoes, and complicated clutter induce modal crosstalk and disrupt inherent modal orthogonality. Additionally, mainstream mature technologies including MIMO radar and multi-beam arrays can realize most information dimensions brought by OAM, which weakens the exclusive technical merits of OAM wave modulation. Figure 5a depicts generalized phase-discontinuity reflection and refraction laws that enable arbitrary interface wavefront shaping; Figure 5b presents ultra-thin planar lenses and axicons constructed via customized spatial phase profiles to realize designated wavefront modulation.

From an objective engineering viewpoint, OAM waves serve only as an auxiliary modulation dimension for mode encoding and feature enhancement under specific radar scenarios, rather than a universal substitute for classic beamforming and phased array architectures.

4.5. Section Summary

In summary, metasurfaces innovate radar beam control and imaging via aperture-level electromagnetic wave manipulation, transforming traditional RF-chain-dependent electromagnetic regulation into a structure–information synergistic paradigm. Leveraging programmable beamforming, dynamic aperture coding, and near-field focusing mechanisms, metasurfaces enable multi-functional aperture reuse and flexible electromagnetic reconfiguration with reduced system overhead. Nevertheless, their practical performance

is still bounded by inherent limitations including bandwidth constraint, power-handling capacity, phase quantization errors, and imperfect system calibration.

From an engineering deployment perspective, the most viable technical route lies in hybrid integration with conventional RF frontends, rather than the full replacement of existing radar architectures. While inheriting mature transceiver hardware chains, programmable metasurface apertures introduce low-cost beam and pattern reconfigurability, achieving optimal trade-offs between system performance and hardware complexity. This evolutionary trend positions electromagnetic metasurfaces as supporting technology for upgrading traditional hardware-fixed radar systems toward electronically reconfigurable or software-controlled electromagnetic aperture architectures.

Despite superior aperture-level wave manipulation flexibility offered by metasurface-based beamforming and imaging, practical radar deployment demands tighter integration with waveform generation, backend signal processing, and multi-task cooperative operation. This drives the technological evolution from discrete electromagnetic function realization to systematic, metasurface-native radar architectural design.

5. Metasurface-Enabled Radar Architectures

Compared with the electromagnetic modulation mechanisms and aperture-level functions discussed in Sections 2–4, recent metasurface prototypes demonstrate the feasibility of transferring selected radar functions, including waveform generation, frequency translation, dechirping, spatial encoding, and harmonic beam control, from conventional circuit-level implementations to programmable electromagnetic apertures. These demonstrations should not be interpreted as the wholesale replacement of mature radar RF chains. Rather, they establish an emerging hybrid architecture in which metasurfaces perform selected front-end functions while conventional sources, amplifiers, antennas, control electronics, data converters, and digital processors remain necessary. Accordingly, this section distinguishes experimentally demonstrated functions from projected system-level benefits and explicitly identifies the performance metrics that have not yet been reported.

By virtue of direct aperture-level electromagnetic field manipulation, metasurfaces migrate partial conventional RF-chain functionalities to the electromagnetic interface, establishing an emerging "aperture-as-processing" paradigm. This architectural innovation transfers certain signal generation, modulation and preprocessing operations from the electronic domain to the electromagnetic domain, fostering a new family of programmable-aperture-centric radar systems. Representative metasurface-based radar architectural frameworks are visualized in Figure 6. This section systematically discusses four typical advanced radar architectures enabled by metasurfaces: time-modulated radar, computational compressed-sensing radar, continuous-aperture MIMO systems, and ISAC platforms.

5.1. Time-Modulated Radar Systems

Time-varying metasurfaces introduce temporal modulation to electromagnetic boundary parameters, transforming conventional linear time-invariant (LTI) electromagnetic systems into linear time-varying (LTV) counterparts. This paradigm empowers aperture-level spectrum shaping and waveform manipulation, which cannot be realized by static metasurfaces [21,35,45]. Such temporal modulation provides an alternative solution to conventional waveform generation architectures that rely on discrete local oscillators, mixers, and analog modulators.

The time-dependent equivalent reflection coefficient of a programmable metasurface is defined as

$$\Gamma(t) = A(t)e^{j\phi(t)} \tag{28}$$

and let the incident continuous-wave signal be

$$E_i(t) = E_0 e^{j\omega_0 t} \tag{29}$$

Then, the reflected field can be expressed as

$$E_r(t) = A(t) E_0 e^{j(\omega_0 t + \phi(t))} \tag{30}$$

Its instantaneous frequency satisfies

$$\omega_{inst}(t) = \omega_0 + \frac{d\phi(t)}{dt} \tag{31}$$

Accordingly, the additional frequency shift introduced by the metasurface is

$$f_{\mathrm{m}}(t) = \frac{1}{2\pi} \frac{\mathrm{d}\phi_{\mathrm{m}}(t)}{\mathrm{d}t}, \tag{32}$$

where f_{m} is the metasurface-induced frequency shift in hertz, and $\phi_{\mathrm{m}}(t)$ is the additional temporal phase imposed by the metasurface in radians. This frequency shift originates from temporal modulation of the electromagnetic boundary rather than from physical target motion.

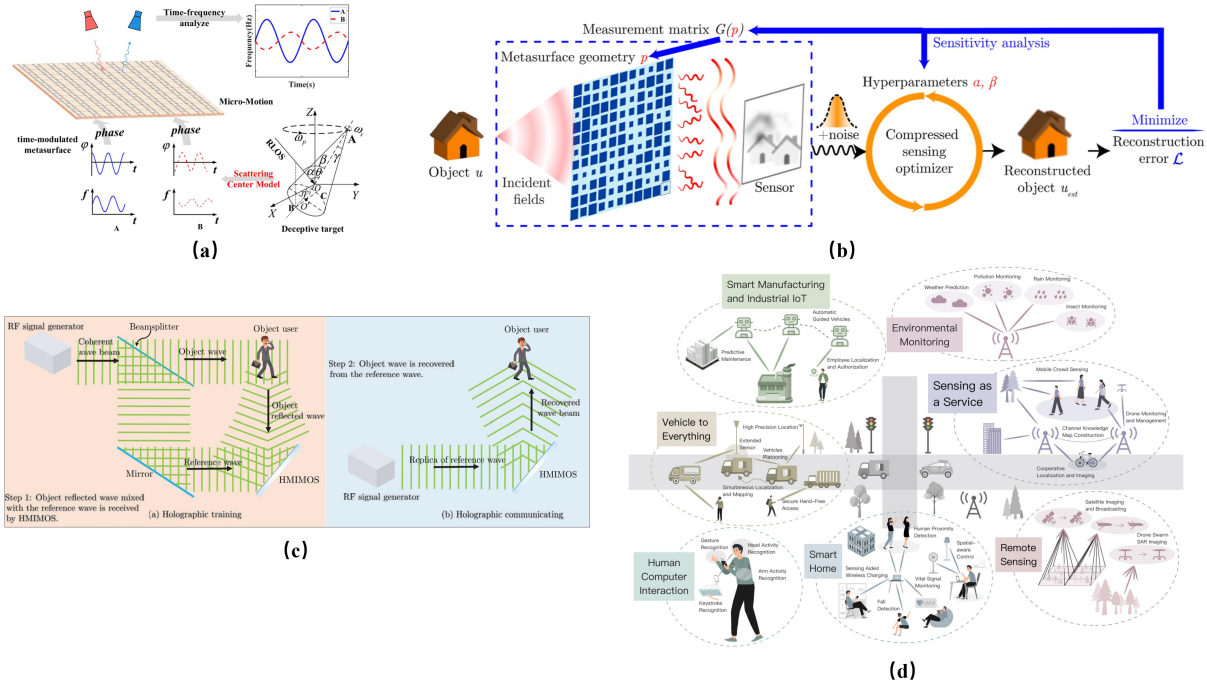


Figure 6. Representative radar-specific and cross-domain architectures relevant to metasurface-enabled radar evolution. (**a**) Time-modulated metasurface for scattering-center-based micromotion false-target generation and micro-Doppler manipulation, reproduced from Ref. [107]. (**b**) End-to-end-optimized optical metasurface imaging pipeline incorporating compressed-sensing reconstruction, presented as a cross-domain analogue for computational radar, reproduced from Ref. [108]. (**c**) Communication-oriented holographic MIMO architecture illustrating continuous-aperture field synthesis and spatial multiplexing, reproduced from Ref. [38]. (**d**) Representative application and service scenarios for ISAC in 6G networks, reproduced from Ref. [109].

Under a narrowband, monostatic, single-bounce radar model, a conventional Doppler processor may interpret f_{m} as an apparent radial velocity:

$$v_{\mathrm{app}} = \frac{\lambda}{2} f_{\mathrm{m}}, \tag{33}$$

where λ is the operating wavelength in meters. The sign of v_{app} depends on the adopted phase convention and the definition of positive radial velocity. This apparent-velocity relation is not directly applicable to general bistatic, multistatic, or wideband radar geometries.

In addition to artificial frequency shifting, a nonlinear temporal phase profile can be used to synthesize frequency-modulated radar waveforms. For example, when a LFM signal $\omega(t) = \omega_0 + \mu t$ is desired, the corresponding phase function is

$$\phi(t) = \int \mu t \, dt = \frac{1}{2} \mu t^2 \tag{34}$$

where $\mu = d\omega/dt$ is the angular chirp rate with units of rad/s^2. If the instantaneous frequency is expressed in Hz as $f(t) = f_0 + Kt$, then $K = df/dt$ is the chirp rate in Hz/s, and the corresponding phase term is $2\pi\left(f_0 t + \frac{1}{2} K t^2\right)$. In Equation (30), the carrier phase $\omega_0 t$ is already included in the incident wave, and $\phi(t)$ denotes the additional phase modulation imposed by the metasurface.

This unique temporal modulation mechanism shifts radar waveform generation from traditional RF-circuit-based synthesis to electromagnetic-aperture-domain programming, establishing the concept of aperture-level waveform synthesis. Figure 6a demonstrates spectrum reshaping and micro-Doppler modulation enabled by time-domain coded metasurfaces.

Recent experiments demonstrate a clear progression from aperture-level waveform synthesis to partial integration of the radar transmit–receive signal chain. Ke et al. experimentally implemented a varactor-loaded space–time-coding metasurface operating at 2.6 GHz, which provided nearly 520° of continuously tunable reflection phase with a measured reflection loss below 2.5 dB [110]. By imposing nonlinear periodic phase profiles with a modulation period of 10 µs, the metasurface directly generated and spatially steered different FMCW waveforms from a single-frequency illumination. This experiment established the feasibility of aperture-domain radar waveform synthesis, although conversion efficiency, phase noise, spectral purity, and available radiated power were not comprehensively reported. More recently, Wang et al. extended this concept to both sides of the radar signal chain by employing separate information metasurfaces at the transmitter and receiver [37]. The transmitting metasurface generated a 1-MHz-bandwidth FMCW signal at 4.12 GHz, whereas the receiving metasurface performed dechirp processing directly in the RF domain, converting broadband echoes into narrowband beat signals before digitization. In an echo-simulator experiment, a stationary target set at 1 km was estimated at 1.09 km, within the reported range resolution of 0.15 km, and range–velocity measurements were further demonstrated for single and multiple targets. These results represent an important transition from isolated waveform manipulation to experimentally validated radar-chain functionality. Nevertheless, the demonstrated system should be interpreted as transferring selected synthesis and preprocessing operations to the metasurface rather than completely replacing the conventional RF chain, because dynamic range, transmitter–receiver isolation, phase noise, conversion efficiency, power consumption, and RF power handling were not fully benchmarked.

A further increase in temporal modulation speed was reported by Qian et al. using a PIN-diode-based time-domain-coding metasurface operating at 4.7 GHz [111]. The experimentally applicable phase-state switching rate reached approximately 50 MHz, correspond-

ing to a 20 ns coding interval. This platform generated FMCW signals with a bandwidth of 10 MHz and a period of 50 µs, yielding a nominal range resolution of 15 m. The measured waveform nonlinearity was below 0.76%, although residual unwanted harmonics remained because of phase-coding errors and the finite transient response of the PIN diodes. Outdoor experiments detected a drone at distances of approximately 50–130 m, and the reported maximum range sidelobe levels were below −13 dB. Compared with the earlier waveform-generation demonstrations, this work substantially increased the modulation bandwidth and moved metasurface-generated FMCW signals toward target range-velocity measurement. However, the experiment was conducted in a relatively uncluttered single-target environment, and further validation is required under multiple-target, low-SNR, interference, and high-power operating conditions.

Taken together, these experiments demonstrate the functional feasibility of aperture-level waveform generation, harmonic beam control, artificial Doppler modulation, and receive-side RF dechirping. However, the demonstrated capabilities should be distinguished from their projected system-level benefits. In particular, relocating waveform synthesis to a programmable metasurface does not imply that the complete RF chain has been removed, because a monochromatic source, illumination antenna, control electronics, bias networks, and downstream signal processing remain necessary. Similarly, receive-side dechirping reduces the analog bandwidth presented to the subsequent receiver, but the corresponding reductions in ADC sampling rate, effective number of bits, data throughput, storage, latency, and power consumption have not yet been quantitatively benchmarked. Across the reported experiments, conversion efficiency, spur-free dynamic range, phase noise, transmitter–receiver isolation, spectral purity, and RF power-handling capability are also reported incompletely. Therefore, the available results support partial functional migration to the aperture rather than complete replacement of conventional radar RF and digital chains [37,110,111]. Table 4 systematically summarizes the core functions, technical advantages, and inherent limitations of time-modulated metasurface radar systems.

Table 4. Radar-oriented functions, benefits, and constraints of time-modulated metasurfaces.

Metasurface Operation	Experimentally Demonstrated Capability	Reported Quantitative Evidence	Projected System-Level Benefit	Unreported Metrics and Limitations
Temporal phase coding [45–47]	Direct FMCW/LFM-like waveform generation and frequency conversion [112]	Improves waveform agility and frequency reconfigurability	Potential reduction in dedicated chirp-synthesis and frequency-conversion hardware	Modulation speed, phase accuracy, and timing synchronization
Space–time coding [45–47]	Harmonic beam steering and multi-frequency radiation	Enables joint spatial–spectral control	Supports aperture multiplexing and multifunctional radar operation	Harmonic leakage, spectral purity, and control complexity
Nonlinear temporal phase modulation [112]	FMCW/LFM-like waveform generation	Enables flexible chirp generation at the aperture	Transfers part of waveform synthesis from RF chains to the metasurface aperture	Phase linearity, modulation bandwidth, and calibration accuracy
Artificial Doppler modulation [113]	Doppler and micro-Doppler signature control	Supports velocity-domain deception and dynamic scattering control	Generates apparent motion signatures without mechanical motion	Requires precise temporal control and stable modulation

Table 4. *Cont.*

Metasurface Operation	Experimentally Demonstrated Capability	Reported Quantitative Evidence	Projected System-Level Benefit	Unreported Metrics and Limitations
Pseudo-random temporal coding [48]	LPI-oriented scattering and spectral spreading	Reduces spectral power density at selected frequencies	Weakens stationary scattering signatures and supports selective camouflage	Bandwidth occupation, receiver coordination, and spectral management
Receive-side temporal coding [44,112]	RF-domain dechirping and range–velocity estimation	Reduces backend sampling and reconstruction burden	Potential reduction in the analog input bandwidth and sampling-rate requirement of the subsequent ADC	Model mismatch, calibration stability, and dynamic range
Time-modulated scattering control [48,113]	Adaptive stealth and anti-radar countermeasures	Improves dynamic RCS reduction and anti-recognition capability	Avoids fixed scattering patterns being learned by cognitive radar	Power handling, nonlinear devices, and thermal reliability
ISAC-oriented temporal coding [38–40,47]	Concurrent communication-beam control and harmonic-assisted direction sensing	Supports waveform sharing and spectral reuse	Potential reuse of a common programmable aperture for communication and sensing	Multi-objective optimization, synchronization, and interference management

Beyond pure radar signal regulation, time-modulated metasurfaces open up a novel route for ISAC implementation. By embedding digital information into temporal modulation sequences, metasurfaces can tailor scattering spectral characteristics while transmitting auxiliary data via harmonic frequency channels. Such frequency-domain multiplexing capability enables multifunctional co-design and supports the emerging integrated radar and communication architectural paradigm.

From a system-level perspective, time-modulated metasurface radar possesses two distinct advantages. First, its waveform generation is digital-controlled, granting superior reconfigurability and fast multi-task switching adaptability. From an architectural perspective, aperture-level waveform synthesis may reduce the number of dedicated waveform-generation and frequency-conversion components in the RF signal path. This potential benefit has been illustrated through simplified functional block diagrams, but quantitative reductions in component count, physical volume, mass, DC power consumption, thermal load, and total system cost have not yet been reported consistently. Therefore, low-profile and lightweight integration should presently be regarded as a projected engineering benefit rather than an experimentally established system-level advantage. Nevertheless, this architectural scheme still faces inherent technical constraints. The maximum modulation speed is bounded by the transient response of active tuning components, which restricts the operational bandwidth. In addition, time synchronization jitter directly converts into phase fluctuation, following the approximate relation

$$\Delta\phi \approx \omega_0 \Delta t \tag{35}$$

Moreover, high-power operation induces nonlinear distortion and parasitic spectral spurs, further degrading spectral purity and system stability. Owing to the above limitations, current time-modulated metasurface radar systems are more applicable to low- and medium-power experimental platforms. Large-scale practical deployment still requires further improvements in power-handling capacity and spectral suppression techniques [41,107,114].

5.2. Computational and Compressive Radar

Beyond flexible waveform generation, metasurfaces enable aperture-level analog signal processing at the receiving end, driving the evolution of radar systems toward computational imaging and compressed sensing paradigms [42,115,116]. The core principle relies on the spatial coding capability of metasurface apertures, which transforms conventional high-dimensional full-scene observation into low-dimensional sampling followed by sparse reconstruction.

Given a scene scattering distribution $x(\mathbf{r})$, the echo measurement corresponding to the m-th metasurface coding state is formulated as

$$y_m = \int G_m(\mathbf{r}) x(\mathbf{r}) d\mathbf{r} + n_m \tag{36}$$

where $G_m(\mathbf{r})$ denotes the system response function governed by the metasurface spatial coding pattern. Stacking all independent sampling outputs yields the matrix measurement model:

$$\mathbf{y} = \mathbf{\Phi x} + \mathbf{n} \tag{37}$$

When the scene signal $\mathbf{x}$ exhibits sparsity in a specific transform domain, high-fidelity scene reconstruction can be achieved via compressed sensing algorithms, which drastically cuts the required sampling quantities [108,117,118].

In addition to coded-aperture measurements, a temporally modulated receive-side metasurface can perform RF-domain dechirping for an FMCW radar. Consider an ideal complex-valued linear FMCW waveform

$$s_{\mathrm{t}}(t) = \exp\left\{ j2\pi \left(f_{\mathrm{c}} t + \frac{1}{2} K t^2 \right) \right\}, \tag{38}$$

where f_{c} is the carrier frequency in hertz, and $K = \mathrm{d}f/\mathrm{d}t$ is the chirp rate in $\mathrm{Hz\,s^{-1}}$. For a stationary point target with complex scattering coefficient α and round-trip propagation delay τ, the received echo is

$$s_{\mathrm{r}}(t) = \alpha \exp\left\{ j2\pi \left[f_{\mathrm{c}}(t-\tau) + \frac{1}{2} K (t-\tau)^2 \right] \right\}. \tag{39}$$

If the receive-side metasurface applies an ideal conjugate temporal response

$$\Gamma_{\mathrm{d}}(t) = \exp\left\{ -j2\pi \left(f_{\mathrm{c}} t + \frac{1}{2} K t^2 \right) \right\}, \tag{40}$$

the output becomes

$$s_{\mathrm{b}}(t) = s_{\mathrm{r}}(t) \Gamma_{\mathrm{d}}(t) \tag{41}$$

$$= \alpha \exp\left[-j2\pi K \tau t - j2\pi f_{\mathrm{c}} \tau + j\pi K \tau^2 \right]. \tag{42}$$

The terms $-2\pi f_{\mathrm{c}} \tau + \pi K \tau^2$ are independent of fast time and therefore constitute a constant phase. The time-dependent term corresponds to a beat frequency of $-K\tau$. Its sign depends on the conjugate-mixing convention, while its magnitude is

$$|f_{\mathrm{b}}| = |K| \tau. \tag{43}$$

The target range is therefore estimated as

$$R = \frac{c\tau}{2} = \frac{c|f_b|}{2|K|}, \tag{44}$$

where c is the propagation speed of electromagnetic waves in free space in $\mathrm{m\,s^{-1}}$, R is the target range in metres, and τ is the round-trip delay in seconds.

This derivation assumes an ideal linear chirp, a stationary point target, a single propagation path, perfect synchronization between the transmitted waveform and the metasurface dechirping sequence, negligible amplitude variation during one chirp, and no Doppler contribution. For a moving target, the beat signal contains an additional Doppler-dependent term and the range–velocity coupling must be treated explicitly. The receive-side dechirping operation therefore converts a broadband FMCW echo into a narrowband beat signal before digitization. This reduces the analog signal bandwidth presented to the subsequent receiver. However, the resulting reductions in ADC sampling rate, effective number of bits, dynamic range, data throughput, storage, latency, and power consumption must be evaluated experimentally and should not be inferred solely from the reduction in signal bandwidth. Figure 6b illustrates the metasurface-based computational imaging architecture that implements aperture-level encoding and low-dimensional sparse reconstruction.

Nevertheless, such computational radar architectures impose stringent constraints on system synchronization precision and dynamic range. Mismatch between transmitting and receiving modulation sequences introduces range deviation and elevated sidelobe levels. In addition, spatial nonuniformity and inter-element mutual coupling in large-scale apertures induce systematic model errors. Accordingly, practical computational radar systems require dedicated calibration and error compensation strategies to guarantee reconstruction accuracy [43,119,120].

5.3. MIMO and Multiplexed Systems

Traditional MIMO radar systems rely on discrete antenna arrays and independent RF chains for spatial sampling, yielding system complexity that scales linearly with the number of array elements. In contrast, metasurfaces leverage continuous aperture modulation and spatial coding to implement mode-division multiplexing, a compelling alternative to conventional element-division multiplexing. This mode-multiplexing framework provides a potential route toward reducing the number of independently controlled radiating elements and RF channels. However, the reduction in hardware complexity depends on the feed topology, the number of simultaneously recoverable modes, channel isolation, calibration accuracy, and the required dynamic range. In the absence of an experimental comparison reporting the RF-channel count, total aperture efficiency, crosstalk, power consumption, and radar detection performance, the hardware reduction should be treated as a projected architectural benefit. [38,39,121].

For a programmable metasurface aperture, the m-th coding state corresponds to a complex weighting function $w_m(\mathbf{r})$, whose far-field radiation pattern is expressed as

$$F_m(\mathbf{k}) = \int w_m(\mathbf{r}) e^{-j\mathbf{k}\cdot\mathbf{r}} d\mathbf{r} \tag{45}$$

If different modes satisfy the approximate orthogonality condition

$$\int_{\Omega_k} F_m(\mathbf{k}) F_n^*(\mathbf{k})\, \mathrm{d}\Omega_k \approx 0, \qquad m \neq n, \tag{46}$$

effective multi-channel spatial multiplexing can be realized.

The above orthogonality relation holds for ideal, independently controlled aperture modes. In practical metasurface MIMO implementations, however, inter-unit electromagnetic coupling, substrate modes, surface wave propagation, and biasing imperfections jointly distort the ideal aperture weighting distribution. Such non-idealities deviate the actual radiation mode $\tilde{w}_m(\mathbf{r})$ from the theoretically designed $w_m(\mathbf{r})$, breaking strict mode orthogonality. The resultant inter-channel crosstalk reduces spatial degrees of freedom and deteriorates target parameter estimation accuracy. As such, coupling-aware full-wave-circuit co-design, array-level amplitude-phase calibration, and mode decoupling algorithms are indispensable for high-performance metasurface MIMO radar operation.

For an electrically large continuous aperture, the number of physically resolvable spatial modes generally scales with the normalized aperture area:

$$N_{\mathrm{DoF}} = \mathcal{O}\left(\frac{A}{\lambda^2}\right). \tag{47}$$

Here, A is the effective aperture area in square meters, and λ is the wavelength in meters. The proportionality coefficient is not universal; it depends on the aperture geometry, polarization model, observable solid angle, propagation regime, and the adopted threshold for mode independence. This physical modal bound should not be interpreted as the number of independent RF channels directly realizable in a practical metasurface radar. By dynamically configuring diverse spatial radiation modes, programmable metasurfaces equip a single continuous physical aperture with multi-channel capabilities comparable to discrete multi-antenna arrays. Figure 6c visualizes the spatial multiplexing and field manipulation principle of continuous-aperture holographic MIMO metasurfaces.

Equation (46) represents an approximate physical upper bound on the spatial degrees of freedom of an ideal continuous aperture. It does not directly specify the number of independently usable radar channels in a practical metasurface system. The realized channel count is further limited by mode correlation, mutual coupling, aperture loss, finite phase resolution, receiver dynamic range, and calibration errors. Therefore, the theoretical degrees-of-freedom advantage should not be interpreted as experimental evidence of an equivalent reduction in RF chains.

While such holographic MIMO architectures substantially reduce RF channel counts and system complexity, their performance fundamentally relies on precise mode orthogonality. In practical engineering scenarios, finite phase quantization, frequency dispersion, and inter-element coupling jointly undermine orthogonal mode isolation and induce residual channel crosstalk. Furthermore, real-time mode synthesis and decoupling involve intensive matrix computation, posing challenges for high-speed radar processing. For these reasons, continuous-aperture MIMO serves as a favorable supplementary technique rather than a full replacement for traditional discrete array systems [90,122,123].

5.4. Integrated Sensing and Communication

Driven by the scarcity of available spectrum and rising demands for integrated multifunctional radio systems, ISAC has emerged as a mainstream evolutionary direction for modern radar technologies. Benefiting from multi-dimensional joint wave modulation, electromagnetic metasurfaces lay solid technical foundations for simultaneous multiplexing of spectral, spatial, and waveform resources [40,109,124].

Within a unified transmit signal framework, the composite radiated waveform is formulated as

$$s(t) = s_{radar}(t) + s_{comm}(t) \tag{48}$$

Metasurfaces map independent radar and communication data streams to separated radiation beams or discrete spectral subbands via joint spatial–temporal coding. Given a time-varying spatial coding matrix $C(t)$, the resultant far-field radiation field follows

$$E(\theta, t) = \sum C_n(t) e^{j\phi_n(\theta)} \tag{49}$$

From an information-theoretic standpoint, the shared ISAC channel adheres to classic Shannon capacity constraints governed by system bandwidth and signal-to-noise ratio (SNR):

$$C = B \log_2(1 + \mathrm{SNR}) \tag{50}$$

Meanwhile, target sensing performance is highly coupled with the condition number of the measurement matrix and the intrinsic structure of echo signals, creating an unavoidable fundamental trade-off between radar detection and data transmission. Figure 6d demonstrates typical metasurface-enabled ISAC and reconfigurable intelligent surface (RIS) hardware architectures oriented toward 6G wireless systems.

Experimental evidence has recently moved space–time-coding metasurface-enabled ISAC beyond conceptual resource sharing. Chen et al. implemented a 16×16, 2-bit reflection-type space–time-coding metasurface operating at 10.3 GHz [125]. The fundamental-frequency component was used to establish a communication link through programmable beam steering, whereas the generated harmonics provided spatial–spectral features for direction-of-arrival estimation. With a PIN-diode switching rate of 64 MHz, a modulation frequency of 2 MHz, and a QPSK symbol rate of 0.5 Mbps, the system achieved beam steering over approximately -60° to $+60^\circ$ and limited the measured direction-of-arrival error to within 3°. The ISAC functionality was further demonstrated in indoor and outdoor experiments. This work therefore provides experimental evidence that sensing information extracted from metasurface-generated harmonics can support real-time communication-beam adaptation on the same physical aperture. Nevertheless, the demonstrated sensing task was primarily angular estimation rather than complete radar range–Doppler detection, and quantitative information on total aperture efficiency, harmonic conversion efficiency, link budget, DC power consumption, and processing latency remains incomplete.

The experiment demonstrates concurrent communication and direction sensing using the fundamental-frequency and harmonic responses of a common space–time-coded aperture. Nevertheless, the prototype still relied on a commercial software-defined radio, frequency-conversion mixers, external antennas, and digital neural-network processing. Therefore, it validates multifunctional aperture reuse rather than complete integration or elimination of the communication and sensing RF chains. In addition, the reported measurements did not provide a complete quantitative comparison of harmonic conversion efficiency, sensing–communication isolation, error-vector magnitude, total DC power, processing latency, aperture efficiency, or range–Doppler detection performance.

Even with metasurface-assisted co-design, an irreconcilable trade-off persists between sensing precision and communication throughput. Cross-interference introduced by overlapping communication modulation and radar echo waveforms, alongside competitive resource scheduling across dual tasks, constitutes the primary bottleneck limiting practical large-scale ISAC deployment [126–128].

5.5. Study-Level Summary of Reported Experimental Metrics

To distinguish mechanism-level potential from experimentally demonstrated radar capability, Table 5 summarizes representative published metasurface-enabled radar systems and subsystems for which measured results are available. The selected studies are organized according to the role of the metasurface in the radar signal chain and their level

of experimental validation, including aperture-level characterization, radar-subsystem demonstration, complete radar experiments, and field validation. Only parameters explicitly reported in the original publications are listed; "N.R." denotes information not reported by the authors. No missing values were inferred from figures or from ideal theoretical models unless the corresponding estimation procedure was explicitly provided in the source publication.

Table 5 reveals a substantial difference in experimental maturity among the reported metasurface-enabled radar technologies. Passive and electrically tunable RCS-control surfaces have generally been validated through aperture-level scattering or absorption measurements, whereas dynamic metasurface antennas have progressed to computational-imaging and mechanically translated SAR experiments. More recent space–time-coding systems have demonstrated a closer integration with the radar signal chain, including direct FMCW generation, receive-side RF dechirping, range–velocity estimation, harmonic-assisted sensing, and multistatic-radar countermeasures.

The reported numerical values should not, however, be interpreted as a direct performance ranking. The studies employ different aperture sizes, illumination conditions, waveform definitions, target distances, calibration procedures, and measurement geometries. In particular, electromagnetic operating bandwidth, generated-waveform bandwidth, and radar-signal bandwidth represent different quantities. Gain, sidelobe level, conversion efficiency, spectral purity, phase noise, dynamic range, isolation, DC power consumption, and RF power-handling capability are also reported inconsistently. The prevalence of unreported entries therefore identifies an important limitation of the existing literature and highlights the need for standardized reporting of aperture-level and radar-system-level metrics.

Taken together, the studies in Table 5 indicate three successive levels of experimental maturity. The systems reported by Ke et al. [110] and Qian et al. [111] primarily demonstrate transmitter-side waveform generation, with the latter increasing the effective state-switching rate to 50 MHz and the generated FMCW bandwidth to 10 MHz. Wang et al. further incorporated both transmitter-side waveform synthesis and receiver-side RF dechirping, thereby demonstrating partial signal-chain integration and range–velocity estimation. Chen et al. [125] and Sun et al. [129] extended space–time coding to higher-level system functions, namely ISAC and multistatic-radar countermeasures. Care is nevertheless required when comparing the numerical values. For example, the 50- and 64-MHz values reported by Qian et al. [111] and Chen et al. [125] describe device-state switching rates, whereas the 1- and 10-MHz values reported in the FMCW experiments describe generated waveform bandwidths. Similarly, the 15 m and 150 m range resolutions were obtained under different waveform bandwidths, measurement configurations, and target simulators. The available evidence therefore demonstrates increasing functional integration but does not yet support a universal performance ranking among the systems.

The absence of a reported metric is not interpreted as evidence of improved performance. In particular, simplified block diagrams are used only to identify which circuit functions are relocated or omitted; they do not establish quantitative reductions in SWaP, cost, latency, or energy consumption. Receive-side dechirping demonstrates reduced signal bandwidth before digitization but not a measured reduction in ADC sampling rate or power unless these quantities are explicitly reported. Likewise, spectral spreading and carrier suppression are classified as LPI-oriented waveform properties rather than evidence of reduced interception probability. Claims of radar deception are limited to the experimentally measured range, velocity, or localization perturbations under the reported test configurations.

Table 5. System-oriented quantitative comparison of representative experimentally demonstrated metasurface-enabled radar systems and subsystems.

Study	Metasurface Role and Validation	Operating Frequency	Aperture and Element Configuration	Reconfiguration and Control Mechanism	Bandwidth, Scanning, and Switching Characteristics	Key Performance and Demonstrated Radar Function
Balci et al. [130]	Target-mounted adaptive absorber; free-space reflection and transmission measurements	Near 10.5 GHz	Large-area graphene capacitor surface; dimensions and element number N.R.	Electrostatic gating of graphene sheet resistance; continuous absorption control; operating voltage below 5 V	Broadband microwave response; numerical bandwidth and switching time N.R.	Electrically tunable reflection suppression up to 50 dB; adaptive microwave absorption and RCS control
Sleasman et al. [43]	Transmit dynamic metasurface aperture; experimental computational microwave imaging	19 GHz	6 cm one-dimensional aperture; eight cELC radiators; 7.5 mm spacing	Two PIN diodes per cELC; binary radiating and non-radiating states	Narrowband operation with multiple electronically generated radiation masks	Experimental scene reconstruction with a 10:1 measurement-compression ratio
Sleasman et al. [131]	Dynamic transmitting aperture in an experimental synthetic-aperture radar	17.5–20.3 GHz	One-dimensional microstrip-fed cELC aperture; element number N.R.	Two diodes per cELC switch the resonator into or out of the operating band	2.8 GHz bandwidth; spotlight, stripmap, and hybrid imaging modes	Experimental two- and three-dimensional SAR imaging
Su et al. [132]	Passive target-side RCS-reduction metasurface; simulated and measured scattering	6.16–41.63 GHz	Defect-lattice metasurface; aperture size and cell number N.R.	Static passive cells based on defect lattices and destructive interference	10 dB RCS-reduction bandwidth of 6.16–41.63 GHz; ratio bandwidth 6.76:1	Measured RCS reduction of at least 10 dB for both incident polarizations
Kozlov et al. [48]	Temporally modulated coating mounted on a moving metal target; closed-loop radar test	1.5 GHz	Coated metal plate with an area of approximately 0.25 m^2	Time-dependent reflection-phase modulation generates a controllable Doppler shift	Operating range approaching 20% fractional bandwidth	Doppler compensation caused the moving-target echo to be rejected as stationary clutter
Ke et al. [110]	Externally illuminated space–time-coding reflector; waveform and beam measurements	2.6 GHz	385.35 mm × 153.25 mm; 8 × 8 cells; eight controlled columns	Varactor-loaded cells; 0–19 V bias; approximately 520° phase range	Over 360° phase coverage from 2.35 to 2.70 GHz; 10-μs modulation period	Reflection loss below 2.5 dB; direct FMCW generation and beam steering
Wang et al. [37]	Information metasurfaces at the transmitter and receiver; indoor radar experiment	4.12 GHz	Eight independently controlled meta-columns with 24 mm spacing	Varactor-loaded cells; 0–13 V bias; reflection-phase range exceeding 2π	1 MHz FMCW bandwidth; 100 μs chirp; 100 and 200 kHz modulation	Range and velocity estimation; a simulated 1 km target was measured at 1.09 km
Chen et al. [125]	Reflection-type space–time-coding metasurface; indoor and outdoor ISAC experiments	10.3 GHz	16 × 16 cells; two PIN diodes per cell	2-bit coding with four nominal 90° phase states	Beam steering from −60° to 60°; PIN switching rate 64 MHz	DOA error approximately 3°; 0.5 Mbps QPSK communication and sensing
Sun et al. [129]	Target-mounted space–time-coding metasurface; multistatic-radar experiment	10.3 GHz	16 × 16 programmable elements	Space–time-programmable reflection and harmonic generation	0.5 MHz TDOA modulation; 0.1 MHz data-fusion modulation; 5 MHz LFM bandwidth	Disruption of TDOA, FDOA, and multi-receiver fusion, producing false target information
Qian et al. [111]	Time-domain-coding metasurface; chamber and outdoor drone-detection experiments	4.7 GHz	3 × 7 cells; 27 mm period; 16 common coding lines	PIN-diode tuning; 200 coding states over 360°; phase resolution below 2°	10 MHz FMCW bandwidth; 50 μs waveform; 50 MHz switching rate	15 m range resolution; drone detection at 50–130 m; sidelobe level below −13 dB

5.6. Section Summary

In summary, embedding multi-dimensional electromagnetic wave manipulation into radar apertures drives a fundamental architectural paradigm transition from RF-chain-centric hardware frameworks to electromagnetic-aperture-native radar systems. Temporal modulation shifts waveform synthesis from electronic-circuit domains to the physical aperture interface; computational metasurface architectures migrate partial analog pre-processing to the front-end wave manipulation layer; continuous-aperture holographic MIMO has been proposed as a potential approach for reducing the number of independently controlled radiating elements or RF channels, although this benefit has not yet been established at the complete-system level; ISAC further unlock multi-task coexistence for multifunctional radio platforms. Figure 7 systematically outlines the evolutionary roadmap and future research directions of metasurface-based radar architectures. These innovative frameworks reveal that metasurfaces do not merely serve as substitutes for discrete RF components but lay the core physical foundation for self-adaptive electromagnetic systems with improved autonomy, intelligent reconfiguration, and flexible mission adaptation. Such multi-dimensional wave regulation capacities underpin a series of next-generation radar operating modes, covering LPI detection, cognitive active sensing, and intelligent electromagnetic countermeasure systems.

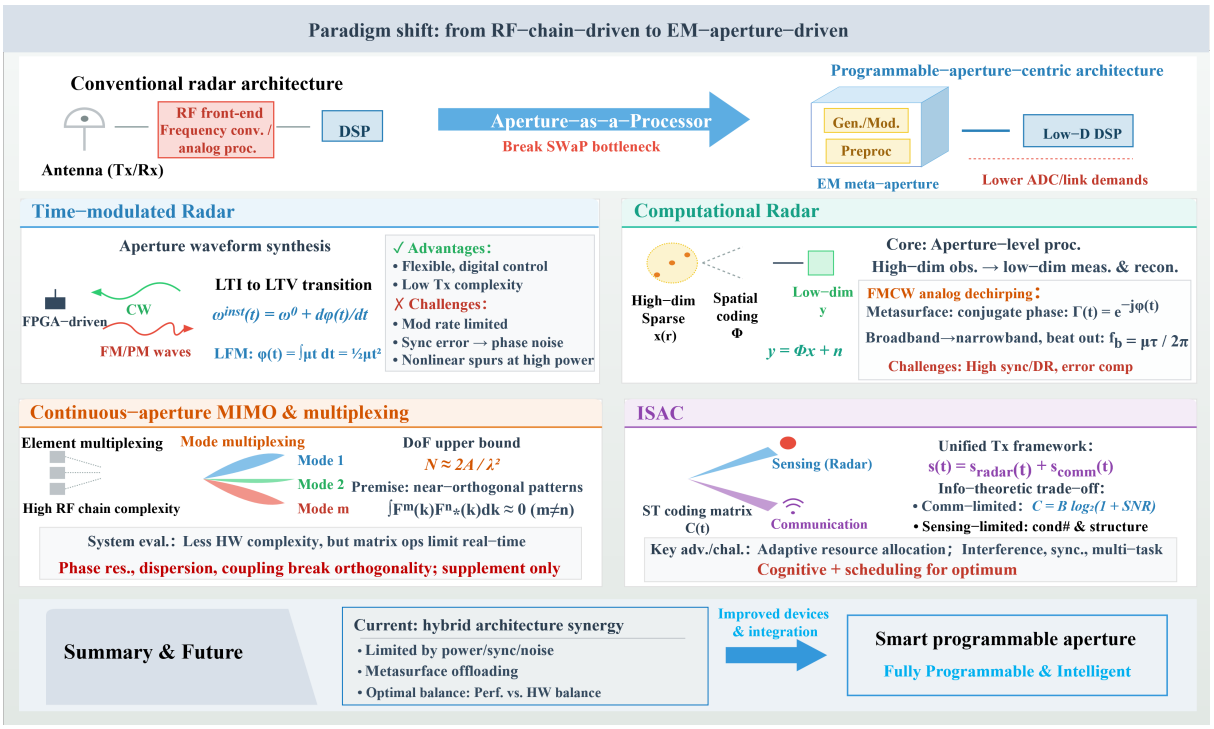


Figure 7. Metasurface-enabled radar architectures.

6. Frontier Applications

With electromagnetic metasurfaces advancing beyond static passive layouts toward programmable, spatiotemporal-modulated and information-intelligent wave manipulation platforms, their functional scope within radar systems extends from basic backscatter suppression to system-wide reconfigurable operation and intelligent sensing paradigms. Faced with intricate electromagnetic confrontation backgrounds and stringent multi-task collaborative demands, metasurfaces deliver potential approach covering radar stealth and jamming deception, low-probability-of-intercept (LPI) detection, cognitive AI-native radar architectures, and multi-modal joint sensing [21,24,133]. Built on the fundamental physical principles and system-level architectural frameworks elaborated in prior sections,

this chapter comprehensively investigates the core functional values and evolutionary tendencies of metasurfaces across the aforementioned cutting-edge radar applications. Figure 8 visualizes a full spectrum of representative frontier application scenarios enabled by electromagnetic metasurfaces.

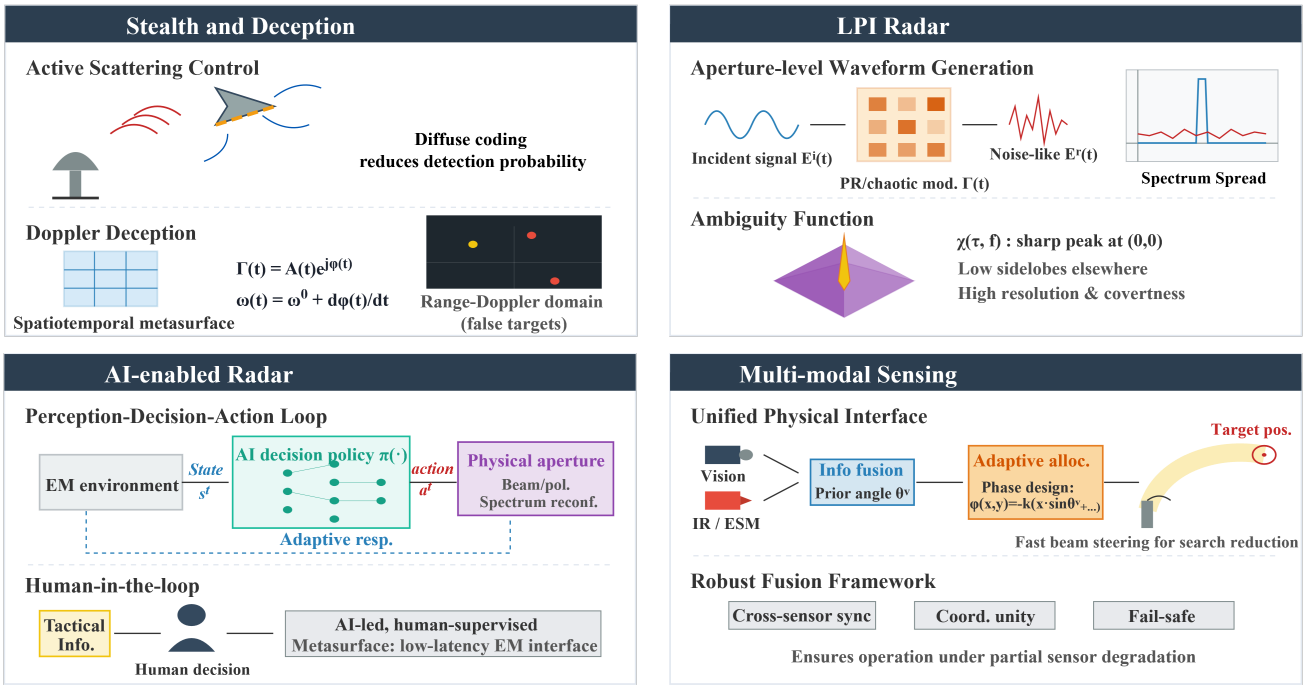


Figure 8. Frontier application scenarios of electromagnetic metasurfaces [21,24,133].

6.1. Stealth and Deception

Electromagnetic metasurfaces establish an innovative paradigm for radar stealth and electronic countermeasure deception, distinct from conventional geometric shaping designs and passive radar-absorbing materials. Their core innovation centers on active scattering engineering via real-time programmable regulation of electromagnetic scattering responses [35,134]. For stealth implementation, collaborative co-design of phase gradient deflection, spatial diffusion coding, and lossy absorption enables metasurfaces to redistribute or dissipate scattered wave energy across angular domains, which suppresses monostatic and multistatic radar detection risks [20,83,135]. Moreover, embedded temporal modulation supports dynamic reconfiguration of scattering fingerprints, rendering time-varying target signatures inconsistent under diverse radar observation perspectives and strengthening the inherent anti-cognitive detection capacity of stealth surfaces [35].

In radar deception scenarios, metasurfaces deliver a native physical-layer modulation channel without full receive–process–retransmit digital relay chains [136]. As derived in Equation (32), a temporal phase gradient imposed by the metasurface produces an additional frequency shift that may be interpreted by a conventional Doppler processor as an apparent target velocity. This fundamental relation reveals that customized temporal phase profiles directly induce artificial frequency offsets during wave scattering, enabling physical-layer Doppler false-target deception [47]. For LFM radar systems, an equivalent beat frequency shift Δf yields an apparent radial range offset approximated as

$$\Delta R \approx \frac{c}{2k}\Delta f \tag{51}$$

where k denotes the linear chirp rate of the transmit waveform [113].

A recent experiment further extended metasurface-based deception from single-radar frequency or range manipulation to countermeasures against multistatic radar localization. Sun et al. mounted a 16×16 space–time-coding metasurface operating at 10.3 GHz on the target and experimentally investigated its influence on time-difference-of-arrival, frequency-difference-of-arrival, and multi-receiver data-fusion localization [129]. For the TDOA experiment, a 0.5 MHz temporal modulation changed the relative delays measured by different receivers and displaced the reconstructed target position. After scaling the measured geometry to a kilometer-level scenario, a target located at approximately $(2.5, 3.9, 0)$ km was reconstructed near $(2.26, 3.53, 0.1)$ km under metasurface modulation. The system was also evaluated using a 5 MHz-bandwidth LFM pulse train for multi-receiver range–Doppler fusion. These results provide experimental evidence that space–time coding can disrupt the cross-receiver consistency on which multistatic localization relies, rather than merely reducing monostatic RCS. However, the kilometer-scale result was obtained through scaled reconstruction based on indoor measurements, and the robustness of the method under unknown receiver geometries, polarization diversity, adaptive waveform changes, and field-level propagation remains to be established.

Furthermore, joint spatial partitioning and temporal phase modulation empower metasurfaces to generate multiple independent virtual targets with decoupled range and velocity signatures across separate angular channels, constructing intricate composite echo distributions within the range–Doppler mapping plane [137]. Such scattering-direct deception architecture boasts ultra-low signal delay and ultra-compact planar hardware compared with digital repeater systems. Nevertheless, its reliable deception performance is constrained by multiple practical limitations: incident electromagnetic field intensity, unit cell power-handling threshold, and multi-dimensional detection capabilities of hostile radar platforms, including multistatic echo coherence verification and polarization discrimination criteria [138,139].

6.2. Metasurface-Enabled LPI-Oriented Waveform Control

LPI radar prioritizes target detection performance while minimizing the interception and recognition risk posed by hostile electronic support measures (ESMs). Its core design principle lies in suppressing signal detectability and enhancing waveform stochasticity [3,140]. Leveraging spatiotemporal modulation and programmable coding, electromagnetic metasurfaces enable aperture-native LPI waveform generation, offering an innovative hardware implementation route for covert radar emission [141].

Low-probability-of-intercept performance is an end-to-end system property rather than a waveform-spectrum property alone. It depends jointly on the transmitted effective isotropic radiated power, antenna directivity, waveform bandwidth, dwell time, scan strategy, propagation loss, hostile-receiver bandwidth and sensitivity, detector type, integration time, and the radar's own processing gain. Therefore, carrier suppression, spectral spreading, or noise-like appearance is neither a necessary nor a sufficient stand-alone measure of operational LPI performance.

Time-modulated and space–time-coded metasurfaces have experimentally demonstrated spectral redistribution, programmable carrier suppression, frequency agility, and pseudo-random scattering modulation. These results establish the feasibility of metasurface-enabled LPI-oriented spectral shaping. For example, pseudo-random temporal coding can redistribute reflected energy from the carrier into multiple spectral components and thereby reduce the power spectral density observed within a selected narrowband channel. However, the reduction depends on the receiver model and may be accompanied by conversion loss, unwanted harmonics, increased occupied bandwidth, and reduced coherent processing gain at the radar receiver.

The ambiguity function characterizes delay–Doppler resolution and sidelobe behavior of the radar waveform, but it does not directly quantify interceptability. A convincing system-level LPI assessment should report, at minimum, the probability of interception or the electronic-support-measure detection probability at a specified false-alarm probability, received power spectral density relative to the receiver noise floor, waveform bandwidth and spectral masks, phase noise and spurious emissions, radar processing gain, matched-filter or coherent-integration loss, and the radar detection probability and detection range under the same emission constraints.

Accordingly, the available metasurface experiments should presently be described as demonstrations of LPI-oriented waveform or scattering control. A claim of experimentally validated LPI radar performance would require a direct comparison with representative intercept receivers while preserving the radar's required target-detection performance.

The backscattered wave modulated by metasurfaces follows

$$E_r(t) = \Gamma(t) E_i(t) \tag{52}$$

When the time-varying reflection coefficient $\Gamma(t)$ is configured with pseudo-random or chaotic characteristics, the resultant radar spectrum undergoes effective spreading and presents noise-like spectral features. Such spectral randomization can reduce the power spectral density observed within a selected receiver bandwidth, but this effect alone does not establish lower interception probability [142]. The time–frequency ambiguity function of the emitted waveform is defined as

$$\chi(\tau, f) = \int s(t) s^*(t - \tau) e^{-j2\pi f t} dt \tag{53}$$

An optimal LPI waveform features a sharp central peak at the zero delay–frequency point and uniformly suppressed low sidelobes across the entire ambiguity plane, realizing favorable balance between imaging resolution and emission covertness [143,144].

Different from conventional LPI waveform generation relying on analog and digital RF chains, metasurface apertures support simultaneous frequency agility, phase randomization, and spatial coding modulation at the electromagnetic interface. This paradigm enables synergistic co-design of waveform diversity and directional radiation control on a single planar aperture [145]. Such electromagnetic-domain waveform reconfiguration fundamentally reduces hardware complexity and lays the technical foundation for dynamically adaptive LPI radar strategies. Nevertheless, practical implementation necessitates deliberate trade-offs between waveform stochasticity and coherent integration gain, together with rigorous spectrum regulation compliance and parasitic harmonic suppression [146].

6.3. Cognitive and AI-Enabled Radar

Cognitive radar realizes environment-adaptive waveform and beam scheduling via a complete closed-loop sensing–decision–execution control framework [8]. Serving as reconfigurable electromagnetic actuators, programmable metasurfaces translate high-level cognitive decision policies into physical aperture modulation, enabling ultrafast reconfiguration of radiation beams, polarization states, and spectral characteristics [147,148]. The whole regulation loop can be abstracted into a state-action Markov decision model formulated as

$$a_t = \pi(s_t) \tag{54}$$

where s_t stands for the instantaneous electromagnetic environmental state, a_t corresponds to the metasurface tuning profile (spatial coding or temporal modulation), and $\pi(\cdot)$ denotes

the intelligent decision policy. Metasurfaces offer a high-dimensional control domain with ultra-low switching latency, supporting instantaneous cross-mode task switching [149].

Artificial intelligence algorithms including neural networks and reinforcement learning greatly expedite the optimization of metasurface coding patterns. By mining the implicit mapping between measured environmental echoes and optimal modulation profiles, the system achieves quasi-real-time aperture reconfiguration to facilitate adaptive beam steering, active interference suppression, and dynamic RCS shaping [150–152]. Nevertheless, AI-enabled cognitive radar architectures still suffer from inherent limitations in environmental generalization, closed-loop control stability, and model physical interpretability. For high-safety, high-reliability radar equipment, multi-domain co-optimization that couples electromagnetic physical boundaries and feedback control theory becomes indispensable [153].

6.4. Human-in-the-Loop Systems

Under intricate electromagnetic confrontation scenarios, fully autonomous intelligent radar systems suffer severe performance degradation under uncertain and dynamically changing interference. For this reason, human–machine collaborative frameworks have evolved into a vital research trend for next-generation radar equipment. As a low-latency electromagnetic interface equipped with abundant modulation freedoms, metasurfaces support instantaneous mapping of human decision commands to aperture-level wave manipulation operations [154].

In typical tactical combat applications, operators can dynamically assign target scattering fingerprints or directional beam profiles according to real-time battlefield situational awareness, with metasurfaces finishing full aperture reconfiguration within millisecond-scale time windows. Such human-in-the-loop collaborative architecture delivers superior operational flexibility and anti-interference robustness against abrupt jamming and time-varying complex electromagnetic backgrounds [155].

From a holistic system design perspective, human–machine cooperative radar architectures must resolve three core bottlenecks: signal transmission latency, intuitive human–machine interface design, and excessive cognitive decision burden, alongside establishing a well-balanced task allocation mechanism between automatic intelligent execution and manual human intervention. The long-term evolutionary roadmap targets hybrid intelligent radar frameworks governed by the "AI-dominant, human-supervised" paradigm, which endows metasurface modulation with instantaneous response speed, tunable reconfigurability, and reliable operational safety simultaneously [156].

6.5. Multi-Modal Sensing

With radar hardware evolving into all-in-one integrated sensing platforms, multi-modal data fusion emerges as a critical technical route to boost overall detection and tracking performance [157]. Relying on flexible programmable modulation capabilities, electromagnetic metasurfaces serve as a unified physical interface that maps heterogeneous multi-sensor data onto aperture-level wave control parameters [158].

For example, in a vision-assisted radar system, the visual sensor provides a prior target angle θ_v, based on which the metasurface designs the phase distribution

Taking vision-aided radar as a representative instance, optical imaging sensors output prior target azimuth and elevation angles θ_v, φ_v. The metasurface accordingly generates the tailored spatial phase profile

$$\phi(x, y) = -k(x \sin\theta_v + y \sin\varphi_v) \tag{55}$$

This customized phase distribution forms directional target-locked beams within microsecond latency and drastically cuts wide-area space scanning overhead [159]. By analogy, measurement data acquired from infrared detectors or electronic support measure (ESM) equipment can also drive real-time metasurface reconfiguration, supporting adaptive allocation of limited spectral and spatial aperture resources.

Even so, cross-modal data fusion inevitably raises extra system overhead stemming from multi-sensor time alignment, unified coordinate calibration, and inconsistent measurement reliability across heterogeneous sensing devices. Accordingly, robust multi-modal fusion architectures and fault-tolerant backup mechanisms must be deployed to sustain stable system operation under partial sensor performance degradation or equipment failure [160].

6.6. Section Summary

Overall, the main advantage of electromagnetic metasurfaces for cutting-edge radar applications stems from their unique identity as programmable electromagnetic interfaces, which realize seamless co-integration of on-aperture waveform synthesis, flexible scattering manipulation, and closed-loop decision control on a unified physical layer [21,161,162]. Covering radar stealth and electronic deception, low-probability-of-intercept (LPI) emission, cognitive intelligent sensing, and multi-modal data fusion, metasurfaces accelerate the paradigm transition of radar hardware from single-purpose detection sensors to versatile multi-task intelligent platforms.

All the above innovative applications exhibit strongly scenario-dependent performance, restricted by complex hostile electromagnetic backgrounds, intrinsic hardware non-idealities, and complicated multi-task collaborative overhead. For this reason, metasurfaces will first serve as auxiliary modules within hybrid radar frameworks, instead of acting as complete replacements for traditional discrete-component radar systems [163–165].

7. Challenges and Future Directions

Despite the remarkable performance gains delivered by electromagnetic metasurfaces across radar wave modulation, tailored scattering control, adaptive beamforming, computational imaging, and programmable aperture architectures, substantial obstacles still block the transformation from lab-scale prototypes to field-deployable radar equipment. Such practical barriers span multi-layer technical dimensions: intrinsic meta-atom electromagnetic characteristics, non-ideal modulation artifacts of active tuning components, full-aperture amplitude–phase calibration errors, thermal dissipation and peak power-handling limits, as well as the difficulty of large-area array integration. From a practical engineering standpoint, this section systematically sorts out these core bottlenecks and explores feasible technical evolution routes toward fully implementable metasurface radar platforms.

7.1. Electromagnetic and Device-Level Bottlenecks

The first category of practical bottlenecks stems from the intrinsic electromagnetic response of meta-atoms and integrated active tuning components, among which limited operational bandwidth and frequency dispersion represent fundamental barriers to radar deployment. Another prominent difficulty lies in the angular robustness of programmable metasurfaces under off-normal oblique incidence. Most meta-unit geometries are designed and characterized under normal illumination with the local periodic approximation assumption [166,167]. In realistic radar operating scenarios, however, incident waves impinge the aperture across a wide angular range due to electronic beam scanning, carrier platform motion, target echo scattering, or multistatic radar layouts. Under oblique illumination,

the equivalent impedance and resonant response of each meta-cell undergo dramatic variation, triggering phase offset drift, amplitude fading, polarization-dependent response, and degraded coding precision [168,169]. Such angular distortion further induces beam pointing deviation, elevated sidelobe levels, suppressed RCS reduction capability, and deteriorated imaging resolution. A series of recent studies on wide-angle robust programmable metasurfaces mitigate such angular sensitivity via broadband meta-atom topology design, balanced electric–magnetic resonant modes, inter-element coupling suppression structures, and angle-robust multi-objective optimization [166,167,170]. Even with these remedies, sustaining stable phase and amplitude responses across wide incident-angle, frequency, and polarization windows remains a critical obstacle for field radar hardware. Most reconfigurable meta-units adopt resonant architectures to realize full 360° phase or amplitude modulation range, whose complex reflection/transmission response follows

$$\Gamma(\omega) = A(\omega)e^{j\phi(\omega)} \tag{56}$$

Frequency-dependent fluctuation of the amplitude envelope $A(\omega)$ and phase term $\phi(\omega)$ introduces severe beam squint, peak gain attenuation, radiation pattern distortion, and waveform deformation within wideband radar systems [15,24,171]. Though non-resonant topologies, geometric phase modulation, and multi-layer stacked laminates partially suppress such frequency dispersion artifacts [172,173], simultaneous attainment of ultra-wide bandwidth, low insertion loss, ultra-thin profile, and continuous dynamic reconfigurability still poses a tough multi-objective trade-off [174,175].

Intrinsic dielectric and conductive loss together with limited aperture efficiency form the second major technical barrier. Passive metasurface layouts suffer from substrate dielectric attenuation, metallic conductor loss, and parasitic surface-wave radiation leakage, while active programmable architectures incur extra insertion loss originating from PIN diodes, varactors, MEMS switching devices, and peripheral bias control circuits. Within radar systems, such cumulative loss not only degrades radiation efficiency and shortens maximum detection range but also aggravates thermal accumulation and drifts in amplitude–phase calibration coefficients.

Power-handling capacity and high-power nonlinear distortion impose stringent restrictions specifically for radar applications, as radar transmitters deliver far higher peak radiated power compared with communication transceivers. Active tuning elements generate nonlinear transfer characteristics under intense electromagnetic field excitation, yielding intermodulation spurs and parasitic spectral harmonics [21,35,176]. For temporally modulated metasurfaces, the spectral distribution of reflected radiation can be formulated as

$$E_r(\omega) = \sum c_n E_i(\omega - n\omega_m) \tag{57}$$

where imperfect time-modulation coefficients produce out-of-band harmonic leakage. These spectral contaminants deteriorate output spectral purity, weaken LPI performance, and impair coherent accumulation gain in radar signal processing [21].

7.2. Practical Implementation Issues for Radar Deployment

Beyond fundamental electromagnetic wave regulation performance, field deployment of metasurface radar systems demands comprehensive engineering optimization across five system-level dimensions: aperture amplitude–phase calibration, inter-element mutual coupling suppression, bias and control network design, thermal dissipation management, and large-array scalability. These engineering bottlenecks determine whether small-scale laboratory meta-surface prototypes can evolve into high-stability, field-adaptable radar hardware platforms.

First, large-area programmable meta-apertures rely on dedicated calibration frameworks that share partial similarities with traditional phased arrays yet differ substantially in implementation logic. Fabrication machining tolerances, drifting bias voltages, temperature variation, and long-term component aging all drive discrepancies between the actual and idealized unit-cell amplitude–phase responses. Such mismatches accumulate spatially over the full aperture and trigger beam pointing bias, elevated sidelobe floors, and spurious imaging artifacts. To sustain consistent radar detection performance, three mainstream correction schemes are widely adopted: lookup-table compensation, near-field full-aperture scanning characterization, and real-time in situ self-calibration.

Second, inter-element electromagnetic mutual coupling constitutes a prominent technical obstacle for densely packed meta-cell layouts. Most coding and beamforming algorithms adopt the ideal independent scattering hypothesis for isolated unit cells. In practical dense meta-arrays, however, each element's radiation signature is perturbed by adjacent resonators, substrate guided modes, parasitic surface waves, and metal bias feed structures. Strong coupling invalidates single-cell simulation models and creates obvious mismatch between numerical predictions and measured radiation/scattering patterns, which necessitates coupling-aware joint full-wave and circuit co-simulation alongside array-wide multi-objective optimization.

Third, DC bias and high-speed control networks are not merely auxiliary peripheral circuits but core functional constituents of programmable metasurface apertures. For metadevices built upon PIN diodes, varactors, or MEMS switches, DC feedlines, RF isolation chokes, metallized vias, external connectors, and switching logic circuits introduce parasitic inductance/capacitance, stray unwanted radiation, and severe electromagnetic crosstalk [92,177,178]. The requirement for timing precision becomes more stringent for temporally modulated metasurfaces, as synchronization jitter directly translates into phase deviation following the approximate relation $\Delta\phi \approx 2\pi f \Delta t$. Such phase distortions degrade beam steering accuracy, target imaging quality, and the gain of coherent signal accumulation [47].

Fourth, thermal dissipation and peak power tolerance must be incorporated into the initial design workflow of radar-dedicated metasurfaces. Lossy absorptive and hybrid metasurfaces intentionally consume partial incident electromagnetic energy, while active reconfigurable architectures generate extra power dissipation inside tuning semiconductors and control circuitry. Persistent thermal buildup shifts resonant operating frequencies, reduces radiation efficiency, induces nonlinear scattering behavior, and accelerates long-term component reliability degradation [147,179,180]. For radar stealth applications, elevated thermal radiation also amplifies infrared target signatures, mandating co-optimization of electromagnetic scattering and thermal transfer characteristics.

Finally, scalable array expansion represents a core practical barrier for radar-grade large apertures. Laboratory demonstrators are generally limited to small meta-cell arrays, whereas real radar missions demand electrically large apertures integrated with thousands to millions of independent tuning units. Aperture scaling imposes tighter manufacturing tolerance limits, raises hardware complexity of multi-channel control, boosts real-time data throughput, exacerbates global synchronization difficulty, and adds tremendous overhead for full-array calibration. Modular tile-based panel architectures, distributed decentralized control, hierarchical multi-stage calibration, and hybrid co-integration with conventional RF frontends serve as viable technical solutions to address the above scaling challenges. Table 6 systematically summarizes all critical engineering implementation constraints, mapping each hardware factor to its corresponding metasurface type, resultant radar performance degradation, and feasible suppression strategies.

Table 6. Practical implementation issues for metasurface-enabled radar deployment.

Limitation	Main Cause	Affected Applications	Radar-Level Consequence	Possible Mitigation
Power handling	Active devices and high peak radar power	Time-modulated radar, programmable beamforming, and active RCS reduction	Nonlinear distortion, breakdown, harmonic pollution, and reliability degradation	High-power devices, passive–active hybrid design, protection circuits, and power derating
Aperture efficiency and insertion loss	Conductor loss, dielectric loss, feed loss, and tuning-device loss	Beam steering, imaging, SAR, and MIMO radar	Reduced gain, shorter detection range, and lower SNR	Low-loss substrates, optimized feed networks, and high-efficiency unit cells
Biasing-network complexity	Dense DC/RF routing, vias, chokes, and switching circuits	Programmable metasurfaces and time-varying metasurfaces	Additional insertion loss, electromagnetic interference, and control latency	Multilayer routing, RF isolation, modular control, and distributed driving circuits
Phase noise and timing jitter	Non-ideal control clocks, switching transients, and synchronization errors	Time-modulated metasurfaces, coherent beamforming, and ISAC	Spectral leakage, beam pointing error, and degraded coherent processing	Low-jitter clocks, synchronization calibration, and timing-error compensation
Thermal management	Absorbed power and active-device heating	Absorptive metasurfaces, hybrid RCS reduction, and active programmable apertures	Resonance drift, efficiency degradation, device aging, and possible infrared signature increase	Thermal simulation, heat-spreading structures, low-loss devices, and thermal-aware design
Mutual coupling	Dense unit-cell spacing, substrate modes, surface waves, and bias lines	Coding metasurfaces, MIMO radar, and large programmable apertures	Mode crosstalk, pattern distortion, and inaccurate scattering prediction	Coupling-aware optimization, full-wave/circuit co-design, and array-level calibration
Calibration stability	Fabrication tolerance, temperature drift, bias fluctuation, and aging	Large-aperture beamforming, imaging, and MIMO systems	Beam pointing error, sidelobe elevation, and imaging artifacts	Near-field calibration, lookup-table correction, and in situ self-calibration
Angular stability	Unit-cell amplitude/phase response varies under oblique incidence	Wide-angle beam steering, conformal apertures, RCS reduction, and multistatic radar	Phase-state drift, sidelobe increase, degraded RCS reduction, and imaging error	Wide-angle meta-atoms, polarization-insensitive design, Huygens-type response, and angle-aware calibration
Manufacturing tolerance	Etching error, assembly deviation, substrate variation, and packaging error	Large passive and programmable apertures	Accumulated phase error and aperture decoherence	Tolerance-aware design, modular testing, and post-fabrication calibration
Environmental robustness	Vibration, humidity, temperature cycling, mechanical deformation, and aging	Airborne, naval, spaceborne, and missile-borne radar platforms	Long-term response drift and reduced operational stability	Robust packaging, environmental testing, and adaptive recalibration

Table 6. *Cont.*

Limitation	Main Cause	Affected Applications	Radar-Level Consequence	Possible Mitigation
ADC/DAC and data interface burden	High bandwidth, temporal coding, large control channels, and real-time updates	Time-modulated radar, ISAC, and computational imaging	High data rate, limited update speed, and digital control bottleneck	Aperture-level preprocessing, hierarchical control, and compressed measurement
Scalability	Large number of unit cells, control channels, and synchronization nodes	Large radar apertures and distributed metasurface panels	High control complexity, calibration burden, and reduced reliability	Tile-based architecture, distributed synchronization, and hierarchical calibration

7.3. Development Pathways and Standardization

To narrow the prominent divide between lab-scale metasurface prototypes and field-deployable radar hardware, follow-up research must shift from discrete single-function verification to cross-domain co-optimization that unifies electromagnetic meta-structures, RF analog circuitry, digital signal processing algorithms, and end-to-end radar mission requirements.

First, hybrid coexistence architectures represent the most feasible short-term engineering route, rather than full replacement of traditional radar frontends. Within such hybrid frameworks, metasurfaces act as programmable sub-aperture arrays, adaptive frequency-selective radomes, reconfigurable scattering modulation skins, or auxiliary sensing apertures, while conventional RF chains deliver stable high-power emission, coherent echo reception, and mature built-in calibration functionality [44,181,182].

Second, multi-physics coupled co-design requires deeper exploration and systematic integration. Radar-specialized metasurface development demands joint optimization across electromagnetic resonant response, circuit parasitic effects, thermal dissipation distribution, mechanical structural deformation, packaging process, and long-term environmental reliability. Such multi-dimensional coupled design is indispensable for airborne, spaceborne, shipborne, and missile-borne radar platforms, where mechanical vibration, drastic temperature fluctuation, high humidity, and strict structural size limits severely degrade aperture electromagnetic performance [135,183,184].

Third, physics-embedded intelligent optimization frameworks will emerge as a dominant research trend. Machine learning algorithms have exhibited great potential for meta-atom inverse design and real-time aperture reconfiguration. Nevertheless, pure data-driven optimization schemes suffer from weak environmental generalization, poor physical interpretability, and insufficient anti-interference robustness under unseen complex electromagnetic backgrounds. Accordingly, future intelligent paradigms ought to fuse analytical physical models, high-fidelity full-wave simulation, measured hardware feedback, and system-level radar detection performance metrics [185,186].

Last, standardized unified evaluation benchmarks are urgently required for fair horizontal comparison. Apart from fundamental electromagnetic indicators including gain, radiation efficiency, operational bandwidth, and scattering suppression level, radar-oriented performance assessment must incorporate mission-oriented metrics: detection probability, false alarm rate, imaging spatial resolution, waveform phase-amplitude fidelity, low-probability-of-intercept (LPI) capability, multistatic anti-interception performance, long-term calibration stability, peak power tolerance, thermal durability, and environmental adaptability [187,188]. Such unified standardized benchmarks facilitate quantitative comparison among diverse metasurface radar implementations and accelerate the

whole industrial transformation from theoretical design to practical engineering deployment [147,189,190].

7.4. Summary

In the short-term engineering roadmap, metasurfaces serve as the most technically viable auxiliary and performance-boosting add-ons for existing radar hardware, covering thin-profile reconfigurable RCS suppression skins, programmable reflectarray/transmitarray apertures, self-adaptive radome layers, dynamic scattering modulation panels, and computational imaging meta-apertures. Such hardware modules can be seamlessly co-integrated with legacy radar frontends without full substitution of well-verified mature RF transceiver chains.

Over the medium-term development window, programmable space–time coding metasurfaces will unlock a broader suite of core active radar functionalities: on-aperture waveform synthesis, harmonic beam agile steering, analog-domain dechirping preprocessing, low-probability-of-intercept oriented scattering shaping, and reconfigurable MIMO/ISAC joint radiation apertures. The full implementation of these capabilities demands substantial improvements in modulation switching speed, long-term calibration stability, phase quantization precision, and overall hardware operational reliability.

For long-term forward-looking research directions, exploratory advanced paradigms cover fully information-native intelligent radar apertures, cognitive self-adaptive metasurface skins, distributed programmable electromagnetic propagation environments, and all-in-one integrated sensing–communication–electronic countermeasure platforms. The engineering maturity of such systems hinges on successive technical breakthroughs across multiple bottleneck metrics: peak power-handling capacity, low insertion loss, high aperture radiation efficiency, global large-array time synchronization, efficient thermal dissipation control, harsh-environment adaptability, and unified radar-system-level performance evaluation standards.

Accordingly, metasurface-augmented radar architectures cannot be regarded as a direct one-to-one replacement for conventional radar equipment within the near future. Hybrid co-integration frameworks constitute a pragmatic evolutionary route: metasurfaces deliver localized space–time electromagnetic reconfigurability at the aperture layer, while traditional radar hardware retains high-power emission capacity, high-fidelity coherent echo reception, and proven robust calibration algorithms [21,24,180,181].

Author Contributions: Writing—original draft preparation, F.G.; Writing—review and editing, K.Z. and Q.Z.; Supervision, L.L. and B.Z. All authors have read and agreed to the published version of the manuscript.

Funding: This study was supported by a research fund from Naval University of Engineering, 2026.

Institutional Review Board Statement: Not applicable.

Informed Consent Statement: Not applicable.

Data Availability Statement: All data analyzed in this study are included in this article.

Acknowledgments: During the preparation of this manuscript, the authors used DeepSeek V4 for language editing and correction of grammatical and stylistic errors. The authors have reviewed and edited the output and take full responsibility for the content of this publication.

Conflicts of Interest: The authors declare no conflicts of interest.

References

1. Skolnik, M.I. (Ed.) *Radar Handbook*, 3rd ed.; McGraw-Hill: New York, NY, USA, 2008.
2. Eaves, J.; Reedy, E. *Principles of Modern Radar*; Springer Science & Business Media: Berlin/Heidelberg, Germany, 2012.

3. Pace, P.E. *Detecting and Classifying Low Probability of Intercept Radar*; Artech House: Norwood, MA, USA, 2009.
4. Fenn, A.J.; Temme, D.H.; Delaney, W.P.; Courtney, W.E. The development of phased-array radar technology. *Linc. Lab. J.* **2000**, *12*, 321–340.
5. Mailloux, R.J. *Phased Array Antenna Handbook*; Artech House: Norwood, MA, USA, 2017.
6. Hasch, J.; Topak, E.; Schnabel, R.; Zwick, T.; Weigel, R.; Waldschmidt, C. Millimeter-wave technology for automotive radar sensors in the 77 GHz frequency band. *IEEE Trans. Microw. Theory Tech.* **2012**, *60*, 845–860. [CrossRef]
7. Zou, X.J.; Wang, Y.W.; Zong, B.F.; Xu, X.G.; Han, L.X.; Zhu, H.; Song, W.; Tan, M.; Du, H.N. Miniaturized low-profile ultrawideband antipodal Vivaldi antenna array loaded with edge techniques. *IEEE Trans. Antennas Propag.* **2026**, *74*, 1156–1161. [CrossRef]
8. Haykin, S. Cognitive radar: A way of the future. *IEEE Signal Process. Mag.* **2006**, *23*, 30–40. [CrossRef]
9. Kingsley, S.; Quegan, S. *Understanding Radar Systems*; SciTech Publishing: Raleigh, NC, USA, 1999.
10. Hassanien, A.; Amin, M.G.; Zhang, Y.D.; Ahmad, F. Dual-function radar-communications: Information embedding using sidelobe control and waveform diversity. *IEEE Trans. Signal Process.* **2015**, *64*, 2168–2181. [CrossRef]
11. Liu, F.; Masouros, C.; Petropulu, A.P.; Griffiths, H.; Hanzo, L. Joint radar and communication design: Applications, state-of-the-art, and the road ahead. *IEEE Trans. Commun.* **2020**, *68*, 3834–3862. [CrossRef]
12. Knott, E.F.; Schaeffer, J.F.; Tulley, M.T. *Radar Cross Section*; SciTech Publishing: Raleigh, NC, USA, 2004.
13. Munk, B.A. *Frequency Selective Surfaces: Theory and Design*; John Wiley & Sons: Hoboken, NJ, USA, 2005.
14. Asadchy, V.S.; Díaz-Rubio, A.; Tretyakov, S.A. Bianisotropic metasurfaces: Physics and applications. *Nanophotonics* **2018**, *7*, 1069–1094. [CrossRef]
15. Yu, N.; Genevet, P.; Kats, M.A.; Aieta, F.; Tetienne, J.P.; Capasso, F.; Gaburro, Z. Light propagation with phase discontinuities: Generalized laws of reflection and refraction. *Science* **2011**, *334*, 333–337. [CrossRef] [PubMed]
16. Kildishev, A.V.; Boltasseva, A.; Shalaev, V.M. Planar photonics with metasurfaces. *Science* **2013**, *339*, 1232009. [CrossRef] [PubMed]
17. Chen, H.T.; Taylor, A.J.; Yu, N. A review of metasurfaces: Physics and applications. *Rep. Prog. Phys.* **2016**, *79*, 076401. [CrossRef] [PubMed]
18. Holloway, C.L.; Kuester, E.F.; Gordon, J.A.; O'Hara, J.F.; Booth, J.C.; Smith, D.R. An overview of the theory and applications of metasurfaces: The two-dimensional equivalents of metamaterials. *IEEE Antennas Propag. Mag.* **2012**, *54*, 10–35. [CrossRef]
19. Mohammadi Estakhri, N.; Alu, A. Wave-front transformation with gradient metasurfaces. *Phys. Rev. X* **2016**, *6*, 041008. [CrossRef]
20. Cui, T.J.; Qi, M.Q.; Wan, X.; Zhao, J.; Cheng, Q.; Lee, K.T.; Lee, J.Y.; Seo, S.; Guo, L.J.; Zhang, Z.; et al. Coding metamaterials, digital metamaterials and programmable metamaterials. *Light. Sci. Appl.* **2014**, *3*, e218. [CrossRef]
21. Zhang, L.; Chen, X.Q.; Liu, S.; Zhang, Q.; Zhao, J.; Dai, J.Y.; Bai, G.D.; Wan, X.; Cheng, Q.; Castaldi, G.; et al. Space-time-coding digital metasurfaces. *Nat. Commun.* **2018**, *9*, 4334. [CrossRef] [PubMed]
22. Li, L.; Cui, T.J. Information metamaterials–from effective media to real-time information processing systems. *Nanophotonics* **2019**, *8*, 703–724. [CrossRef]
23. Shaltout, A.M.; Shalaev, V.M.; Brongersma, M.L. Spatiotemporal light control with active metasurfaces. *Science* **2019**, *364*, eaat3100. [CrossRef] [PubMed]
24. Cui, T.J.; Liu, S.; Zhang, L. Information metamaterials and metasurfaces. *J. Mater. Chem. C* **2017**, *5*, 3644–3668. [CrossRef]
25. Tsilipakos, O.; Tasolamprou, A.C.; Pitilakis, A.; Liu, F.; Wang, X.; Mirmoosa, M.S.; Tzarouchis, D.C.; Abadal, S.; Taghvaee, H.; Liaskos, C.; et al. Toward intelligent metasurfaces: The progress from globally tunable metasurfaces to software-defined metasurfaces with an embedded network of controllers. *Adv. Opt. Mater.* **2020**, *8*, 2000783. [CrossRef]
26. Murugesan, A.; Selvan, K.T.; Iyer, A.K.; Srivastava, K.V.; Alphones, A. A review of metasurface-assisted RCS reduction techniques. *Prog. Electromagn. Res. B* **2021**, *94*, 75–103. [CrossRef]
27. Zhang, L.; Cui, T.J. Space-time-coding digital metasurfaces: Principles and applications. *Research* **2021**, *2021*, 9802673. [CrossRef] [PubMed]
28. Saifullah, Y.; He, Y.; Boag, A.; Yang, G.M.; Xu, F. Recent progress in reconfigurable and intelligent metasurfaces: A comprehensive review of tuning mechanisms, hardware designs, and applications. *Adv. Sci.* **2022**, *9*, 2203747. [CrossRef] [PubMed]
29. Abdelraouf, O.A.M.; Wang, Z.; Liu, H.; Dong, Z.; Wang, Q.; Ye, M.; Wang, X.R.; Wang, Q.J.; Liu, H. Recent advances in tunable metasurfaces: Materials, design, and applications. *ACS Nano* **2022**, *16*, 13339–13369. [CrossRef] [PubMed]
30. Liu, C.; Yang, F.; Xu, S.; Li, M. Reconfigurable metasurface: A systematic categorization and recent advances. *Electromagn. Sci.* **2023**, *1*, 0040021. [CrossRef]
31. Ullah, M.U.; Bin Abdul Latef, T.; Othman, M.; Hussein, M.I.; Alkhoori, H.M.; Yamada, Y.; Kamardin, K.; Khalid, R. A progression in the techniques of reducing RCS for the targets. *Alex. Eng. J.* **2024**, *100*, 153–169. [CrossRef]
32. Shittu, I.; Abou-Khousa, M.; Viegas, J.; Hernandez-Figueroa, H.E.; Elfadel, I.M. Radar cross section reduction metamaterials: A review of principles, design methods, and applications beyond. *IEEE Aerosp. Electron. Syst. Mag.* **2026**, *41*, 4–30. [CrossRef]
33. Pfeiffer, C.; Grbic, A. Metamaterial Huygens' surfaces: Tailoring wave fronts with reflectionless sheets. *Phys. Rev. Lett.* **2013**, *110*, 197401. [CrossRef] [PubMed]

34. Chen, H.; Wang, J.; Ma, H.; Qu, S.; Xu, Z.; Zhang, A.; Yan, M.; Li, Y. Ultra-Wideband Polarization Conversion Metasurfaces Based on Multiple Plasmon Resonances. *J. Appl. Phys.* **2014**, *115*, 154504. [CrossRef]
35. Zhao, J.; Yang, X.; Dai, J.Y.; Cheng, Q.; Li, X.; Qi, N.H.; Ke, J.C.; Bai, G.D.; Liu, S.; Jin, S.; et al. Programmable time-domain digital-coding metasurface for non-linear harmonic manipulation and new wireless communication systems. *Natl. Sci. Rev.* **2019**, *6*, 231–238. [CrossRef] [PubMed]
36. He, Q.; Sun, S.; Zhou, L. Tunable/Reconfigurable Metasurfaces: Physics and Applications. *Research* **2019**, *2019*, 1849272. [CrossRef] [PubMed]
37. Wang, S.R.; Chen, Z.Y.; Chen, S.N.; Dai, J.Y.; Zhang, J.W.; Qi, Z.J.; Wu, L.J.; Sun, M.K.; Zhou, Q.Y.; Li, H.D.; et al. Simplified Radar Architecture Based on Information Metasurface. *Nat. Commun.* **2025**, *16*, 6505. [CrossRef] [PubMed]
38. Huang, C.; Hu, S.; Alexandropoulos, G.C.; Zappone, A.; Yuen, C.; Zhang, R.; Di Renzo, M.; Debbah, M. Holographic MIMO surfaces for 6G wireless networks: Opportunities, challenges, and trends. *IEEE Wirel. Commun.* **2020**, *27*, 118–125. [CrossRef]
39. Björnson, E.; Wymeersch, H.; Matthiesen, B.; Popovski, P.; Sanguinetti, L.; de Carvalho, E. Reconfigurable intelligent surfaces: A signal processing perspective with wireless applications. *IEEE Signal Process. Mag.* **2022**, *39*, 135–158. [CrossRef]
40. Magbool, A.; Kumar, V.; Wu, Q.; Di Renzo, M.; Flanagan, M.F. A Survey on Integrated Sensing and Communication with Intelligent Metasurfaces: Trends, Challenges, and Opportunities. *IEEE Open J. Commun. Soc.* **2025**, *6*, 7270–7318. [CrossRef]
41. Bai, X.; Zhang, F.; Sun, L.; Cao, A.; Zhang, J.; He, C.; Liu, L.; Yao, J.; Zhu, W. Time-Modulated Transmissive Programmable Metasurface for Low-Sidelobe Beam Scanning. *Research* **2022**, *2022*, 9825903. [CrossRef] [PubMed]
42. Hunt, J.; Driscoll, T.; Mrozack, A.; Lipworth, G.; Reynolds, M.; Brady, D.; Smith, D.R. Metamaterial apertures for computational imaging. *Science* **2013**, *339*, 310–313. [CrossRef] [PubMed]
43. Sleasman, T.; Imani, M.F.; Gollub, J.N.; Smith, D.R. Dynamic Metamaterial Aperture for Microwave Imaging. *Appl. Phys. Lett.* **2015**, *107*, 204104. [CrossRef]
44. Imani, M.F.; Gollub, J.N.; Yurduseven, O.; Diebold, A.V.; Boyarsky, M.; Fromenteze, T.; Pulido-Mancera, L.; Sleasman, T.; Smith, D.R. Review of metasurface antennas for computational microwave imaging. *IEEE Trans. Antennas Propag.* **2020**, *68*, 1860–1875. [CrossRef]
45. Taravati, S.; Eleftheriades, G.V. Microwave space-time-modulated metasurfaces. *ACS Photonics* **2022**, *9*, 305–318. [CrossRef]
46. Hadad, Y.; Sounas, D.L.; Alu, A. Space-time gradient metasurfaces. *Phys. Rev. B* **2015**, *92*, 100304. [CrossRef]
47. Ramaccia, D.; Sounas, D.L.; Alu, A.; Toscano, A.; Bilotti, F. Phase-induced frequency conversion and Doppler effect with time-modulated metasurfaces. *IEEE Trans. Antennas Propag.* **2019**, *68*, 1607–1617. [CrossRef]
48. Kozlov, V.; Vovchuk, D.; Ginzburg, P. Broadband Radar Invisibility with Time-Dependent Metasurfaces. *Sci. Rep.* **2021**, *11*, 14187. [CrossRef] [PubMed]
49. Zhu, Y.; Fang, X.; Li, M.; Ramaccia, D.; Toscano, A.; Bilotti, F.; Ding, D. Time-Frequency-Modulated Metasurface for False-Target Generation in Symmetrical Triangular LFM Continuous-Wave Radars. *IEEE Trans. Microw. Theory Tech.* **2025**, *73*, 2531–2543. [CrossRef]
50. Yu, N.; Capasso, F. Flat optics with designer metasurfaces. *Nat. Mater.* **2014**, *13*, 139–150. [CrossRef] [PubMed]
51. Caloz, C.; Deck-Léger, Z.L. Spacetime metamaterials—Part I: General concepts. *IEEE Trans. Antennas Propag.* **2019**, *68*, 1569–1582. [CrossRef]
52. Born, M.; Wolf, E. *Principles of Optics: Electromagnetic Theory of Propagation, Interference and Diffraction of Light*; Elsevier: Amsterdam, The Netherlands, 2013.
53. Ni, X.; Emani, N.K.; Kildishev, A.V.; Boltasseva, A.; Shalaev, V.M. Broadband light bending with plasmonic nanoantennas. *Science* **2012**, *335*, 427. [CrossRef] [PubMed]
54. Kuester, E.F.; Mohamed, M.A.; Piket-May, M.; Holloway, C.L. Averaged transition conditions for electromagnetic fields at a metafilm. *IEEE Trans. Antennas Propag.* **2003**, *51*, 2641–2651. [CrossRef]
55. Paquay, M.; Iriarte, J.C.; Ederra, I.; Gonzalo, R.; de Maagt, P. Thin AMC structure for radar cross-section reduction. *IEEE Trans. Antennas Propag.* **2007**, *55*, 3630–3638. [CrossRef]
56. Aieta, F.; Genevet, P.; Kats, M.A.; Yu, N.; Blanchard, R.; Gaburro, Z.; Capasso, F. Aberration-free ultrathin flat lenses and axicons at telecom wavelengths based on plasmonic metasurfaces. *Nano Lett.* **2012**, *12*, 4932–4936. [CrossRef] [PubMed]
57. Zheng, G.; Mühlenbernd, H.; Kenney, M.; Li, G.; Zentgraf, T.; Zhang, S. Metasurface holograms reaching 80% efficiency. *Nat. Nanotechnol.* **2015**, *10*, 308–312. [CrossRef] [PubMed]
58. Arbabi, E.; Arbabi, A.; Kamali, S.M.; Horie, Y.; Faraon, A. Multiwavelength polarization-insensitive lenses based on dielectric metasurfaces with meta-molecules. *Optica* **2016**, *3*, 628–633. [CrossRef]
59. Díaz-Rubio, A.; Asadchy, V.S.; Elsakka, A.; Tretyakov, S.A. From the generalized reflection law to the realization of perfect anomalous reflectors. *Sci. Adv.* **2017**, *3*, e1602714. [CrossRef] [PubMed]
60. Landy, N.I.; Sajuyigbe, S.; Mock, J.J.; Smith, D.R.; Padilla, W.J. Perfect metamaterial absorber. *Phys. Rev. Lett.* **2008**, *100*, 207402. [CrossRef] [PubMed]

61. Watts, C.M.; Liu, X.; Padilla, W.J. Metamaterial electromagnetic wave absorbers. *Adv. Mater.* **2012**, *24*, OP98–OP120. [CrossRef] [PubMed]
62. Ra'di, Y.; Simovski, C.R.; Tretyakov, S.A. Thin perfect absorbers for electromagnetic waves: Theory, design, and realizations. *Phys. Rev. Appl.* **2015**, *3*, 037001. [CrossRef]
63. Sui, S.; Ma, H.; Wang, J.; Pang, Y.; Feng, M.; Xu, Z.; Qu, S. Absorptive coding metasurface for further radar cross section reduction. *J. Phys. D Appl. Phys.* **2018**, *51*, 065603. [CrossRef]
64. Han, T.; Cao, X.Y.; Gao, J.; Zhao, Y.L.; Zhao, Y. A coding metasurface with properties of absorption and diffusion for RCS reduction. *Prog. Electromagn. Res. C* **2017**, *75*, 181–191. [CrossRef]
65. Lv, Q.; Jin, C.; Zhang, B.; Shen, Z. Hybrid absorptive-diffusive frequency selective radome. *IEEE Trans. Antennas Propag.* **2020**, *69*, 3312–3321. [CrossRef]
66. Zheng, Q.; Guo, C.; Li, H.; Ding, J. Broadband radar cross-section reduction using polarization conversion metasurface. *Int. J. Microw. Wirel. Technol.* **2018**, *10*, 197–206. [CrossRef]
67. Liu, Y.; Hao, Y.; Li, K.; Gong, S. Radar cross section reduction of a microstrip antenna based on polarization conversion metamaterial. *IEEE Antennas Wirel. Propag. Lett.* **2015**, *15*, 80–83. [CrossRef]
68. Ameri, E.; Esmaeli, S.H.; Sedighy, S.H. Ultra wideband radar cross section reduction by using polarization conversion metasurfaces. *Sci. Rep.* **2019**, *9*, 478. [CrossRef] [PubMed]
69. Anwar, R.S.; Mao, L.; Ning, H. Frequency selective surfaces: A review. *Appl. Sci.* **2018**, *8*, 1689. [CrossRef]
70. Rouhi, K.; Rajabalipanah, H.; Abdolali, A. Multi-bit graphene-based bias-encoded metasurfaces for real-time terahertz wavefront shaping: From controllable orbital angular momentum generation toward arbitrary beam tailoring. *Carbon* **2019**, *149*, 125–138. [CrossRef]
71. Huang, C.; Yang, J.; Wu, X.; Song, J.; Pu, M.; Wang, C.; Luo, X. Reconfigurable metasurface cloak for dynamical electromagnetic illusions. *ACS Photonics* **2017**, *5*, 1718–1725. [CrossRef]
72. Cui, T.J.; Liu, S.; Li, L.L. Information entropy of coding metasurface. *Light. Sci. Appl.* **2016**, *5*, e16172. [CrossRef] [PubMed]
73. Li, Y.B.; Li, L.L.; Xu, B.B.; Wu, W.; Wu, R.Y.; Wan, X.; Cheng, Q.; Cui, T.J. Transmission-type 2-bit programmable metasurface for single-sensor and single-frequency microwave imaging. *Sci. Rep.* **2016**, *6*, 23731. [CrossRef] [PubMed]
74. Jones, R.C. A new calculus for the treatment of optical systems I. Description and discussion of the calculus. *J. Opt. Soc. Am.* **1941**, *31*, 488–493. [CrossRef]
75. Grady, N.K.; Heyes, J.E.; Chowdhury, D.R.; Zeng, Y.; Reiten, M.T.; Azad, A.K.; Taylor, A.J.; Dalvit, D.A.R.; Chen, H.T. Terahertz metamaterials for linear polarization conversion and anomalous refraction. *Science* **2013**, *340*, 1304–1307. [CrossRef] [PubMed]
76. Wang, C.; Xu, H.X.; Zhu, R.; Ding, H.; Li, B.; Wang, X.; Yang, C.; Lu, Y. 3-D-printed pentahedral polarization-division transmissive metadevice with versatile wavefronts. *IEEE Trans. Antennas Propag.* **2026**, *74*, 4915–4920. [CrossRef]
77. Huang, L.; Chen, X.; Muhlenbernd, H.; Li, G.; Bai, B.; Tan, Q.; Jin, G.; Zentgraf, T.; Zhang, S. Dispersionless phase discontinuities for controlling light propagation. *Nano Lett.* **2012**, *12*, 5750–5755. [CrossRef] [PubMed]
78. Karimi, E.; Schulz, S.A.; De Leon, I.; Qassim, H.; Upham, J.; Boyd, R.W. Generating optical orbital angular momentum at visible wavelengths using a plasmonic metasurface. *Light. Sci. Appl.* **2014**, *3*, e167. [CrossRef]
79. Arbabi, A.; Horie, Y.; Bagheri, M.; Faraon, A. Dielectric metasurfaces for complete control of phase and polarization with subwavelength spatial resolution and high transmission. *Nat. Nanotechnol.* **2015**, *10*, 937–943. [CrossRef] [PubMed]
80. Galiffi, E.; Tirole, R.; Yin, S.; Li, H.; Vezzoli, S.; Huidobro, P.A.; Silveirinha, M.G.; Sapienza, R.; Alù, A.; Pendry, J.B. Photonics of time-varying media. *Adv. Photonics* **2022**, *4*, 014002. [CrossRef]
81. Ishimaru, A. *Electromagnetic Wave Propagation, Radiation, and Scattering: From Fundamentals to Applications*; John Wiley & Sons: Hoboken, NJ, USA, 2017.
82. Su, J.; Lu, Y.; Liu, J.; Yang, Y.; Li, Z.; Song, J. A novel checkerboard metasurface based on optimized multielement phase cancellation for superwideband RCS reduction. *IEEE Trans. Antennas Propag.* **2018**, *66*, 7091–7099. [CrossRef]
83. Gao, L.H.; Cheng, Q.; Yang, J.; Ma, S.J.; Zhao, J.; Liu, S.; Chen, H.B.; He, Q.; Jiang, W.X.; Ma, H.F.; et al. Broadband diffusion of terahertz waves by multi-bit coding metasurfaces. *Light. Sci. Appl.* **2015**, *4*, e324. [CrossRef]
84. Shao, R.W.; Wu, J.W.; Wang, Z.X.; Xu, H.; Yang, H.Q.; Cheng, Q.; Cui, T.J. Macroscopic model and statistical model to characterize electromagnetic information of a digital coding metasurface. *Natl. Sci. Rev.* **2024**, *11*, nwad299. [CrossRef] [PubMed]
85. Galarregui, J.C.I.; Pereda, A.T.; De Falcon, J.L.M.; Ederra, I.; Gonzalo, R.; de Maagt, P. Broadband radar cross-section reduction using AMC technology. *IEEE Trans. Antennas Propag.* **2013**, *61*, 6136–6143. [CrossRef]
86. Chen, W.; Balanis, C.A.; Birtcher, C.R. Checkerboard EBG surfaces for wideband radar cross section reduction. *IEEE Trans. Antennas Propag.* **2015**, *63*, 2636–2645. [CrossRef]
87. Modi, A.Y.; Balanis, C.A.; Birtcher, C.R.; Shaman, H.N. Novel design of ultrabroadband radar cross section reduction surfaces using artificial magnetic conductors. *IEEE Trans. Antennas Propag.* **2017**, *65*, 5406–5417. [CrossRef]
88. Zheng, Y.; Gao, J.; Cao, X.; Yuan, Z.; Yang, H. Wideband RCS reduction of a microstrip antenna using artificial magnetic conductor structures. *IEEE Antennas Wirel. Propag. Lett.* **2015**, *14*, 1582–1585. [CrossRef]

89. Liu, S.; Cui, T.J.; Xu, Q.; Bao, D.; Du, L.; Wan, X.; Tang, W.X.; Ouyang, C.; Zhou, X.Y.; Yuan, H.; et al. Anisotropic coding metamaterials and their powerful manipulation of differently polarized terahertz waves. *Light. Sci. Appl.* **2016**, *5*, e16076. [CrossRef] [PubMed]
90. Li, L.; Cui, T.J.; Ji, W.; Liu, S.; Ding, J.; Wan, X.; Li, Y.B.; Jiang, M.; Qiu, C.W.; Zhang, S. Electromagnetic reprogrammable coding-metasurface holograms. *Nat. Commun.* **2017**, *8*, 197. [CrossRef] [PubMed]
91. Wu, R.Y.; Shi, C.B.; Liu, S.; Wu, W.; Cui, T.J. Addition theorem for digital coding metamaterials. *Adv. Opt. Mater.* **2018**, *6*, 1701236. [CrossRef]
92. Wu, H.; Bai, G.D.; Liu, S.; Li, L.; Wan, X.; Cheng, Q.; Cui, T.J. Information theory of metasurfaces. *Natl. Sci. Rev.* **2020**, *7*, 561–571. [CrossRef] [PubMed]
93. Jidi, L.; Cao, X.; Tang, Y.; Wang, S.; Zhao, Y.; Zhu, X. A new coding metasurface for wideband RCS reduction. *Radioengineering* **2018**, *27*, 395. [CrossRef]
94. Liang, L.; Wei, M.; Yan, X.; Wei, D.; Liang, D.; Han, J.; Ding, X.; Zhang, G.; Yao, J. Broadband and wide-angle RCS reduction using a 2-bit coding ultrathin metasurface at terahertz frequencies. *Sci. Rep.* **2016**, *6*, 39252. [CrossRef] [PubMed]
95. Zhang, S.; An, Q.; Li, D.; Chen, K.; Zhao, J.; Jiang, T.; Liao, W.; Liu, T.; Feng, Y. A low-RCS coding metasurface utilizing 3-D printed ABS shells and carbonyl iron powder/polyimide composite patches via hybrid mechanisms. *Mater. Horiz.* **2026**, *13*, 4634–4642. [CrossRef] [PubMed]
96. Zhang, S.; Chen, K.; Jiang, T.; Zhao, J.; Feng, Y. A low-RCS and high-gain Fabry-Pérot antenna based on hybrid absorptive-diffusive metasurface. In *Proceedings of the 2024 IEEE International Conference on Computational Electromagnetics (ICCEM)*; IEEE: New York, NY, USA, 2024; pp. 1–3.
97. Hao, J.; Yuan, Y.; Ran, L.; Jiang, T.; Kong, J.A.; Chan, C.T.; Zhou, L. Manipulating electromagnetic wave polarizations by anisotropic metamaterials. *Phys. Rev. Lett.* **2007**, *99*, 063908. [CrossRef] [PubMed]
98. Tian, J.; Wang, X.; Liang, Z.; Gao, Y.; Wang, C.; Han, L. A low-profile polarization conversion metasurface array antenna with broadband RCS reduction. *Prog. Electromagn. Res. Lett.* **2026**, *129*, 59–66. [CrossRef]
99. Sun, S.; He, Q.; Xiao, S.; Xu, Q.; Li, X.; Zhou, L. Gradient-index meta-surfaces as a bridge linking propagating waves and surface waves. *Nat. Mater.* **2012**, *11*, 426–431. [CrossRef] [PubMed]
100. Boyarsky, M.; Sleasman, T.; Pulido-Mancera, L.; Fromenteze, T.; Pedross-Engel, A.; Watts, C.M.; Imani, M.F.; Reynolds, M.S.; Smith, D.R. Synthetic aperture radar with dynamic metasurface antennas: A conceptual development. *J. Opt. Soc. Am. A* **2017**, *34*, A22–A36. [CrossRef] [PubMed]
101. Grbic, A.; Eleftheriades, G.V. Overcoming the diffraction limit with a planar left-handed transmission-line lens. *Phys. Rev. Lett.* **2004**, *92*, 117403. [CrossRef] [PubMed]
102. Hum, S.V.; Perruisseau-Carrier, J. Reconfigurable reflectarrays and array lenses for dynamic antenna beam control: A review. *IEEE Trans. Antennas Propag.* **2013**, *62*, 183–198. [CrossRef]
103. Lustig, M.; Donoho, D.L.; Santos, J.M.; Pauly, J.M. Compressed sensing MRI. *IEEE Signal Process. Mag.* **2008**, *25*, 72–82. [CrossRef]
104. Watts, C.M.; Shrekenhamer, D.; Montoya, J.; Lipworth, G.; Hunt, J.; Sleasman, T.; Krishna, S.; Smith, D.R.; Padilla, W.J. Terahertz compressive imaging with metamaterial spatial light modulators. *Nat. Photonics* **2014**, *8*, 605–609. [CrossRef]
105. Zheng, Q.; Li, Y.; Han, Y.; Feng, M.; Pang, Y.; Wang, J.; Ma, H.; Qu, S.; Zhang, J. Efficient orbital angular momentum vortex beam generation by generalized coding metasurface. *Appl. Phys. A* **2019**, *125*, 136. [CrossRef]
106. Ahmed, H.; Kim, H.; Zhang, Y.; Intaravanne, Y.; Jang, J.; Rho, J.; Chen, S.; Chen, X. Optical metasurfaces for generating and manipulating optical vortex beams. *Nanophotonics* **2022**, *11*, 941–956. [CrossRef] [PubMed]
107. Hou, Y.; Zhu, Y.; Li, M.; Chen, R.; Ding, D.; Khakhomov, S.; Semchenko, I. Scattering-center-model-inspired micromotion false target generation using time-modulated metasurface. *IEEE Antennas Wirel. Propag. Lett.* **2024**, *23*, 4273–4277. [CrossRef]
108. Arya, G.; Li, W.F.; Roques-Carmes, C.; Soljačić, M.; Johnson, S.G.; Lin, Z. End-to-end optimization of metasurfaces for imaging with compressed sensing. *ACS Photonics* **2024**, *11*, 2077–2087. [CrossRef]
109. Liu, F.; Cui, Y.; Masouros, C.; Xu, J.; Han, T.X.; Eldar, Y.C.; Buzzi, S. Integrated sensing and communications: Toward dual-functional wireless networks for 6G and beyond. *IEEE J. Sel. Areas Commun.* **2022**, *40*, 1728–1767. [CrossRef]
110. Ke, J.C.; Dai, J.Y.; Zhang, J.W.; Chen, Z.; Chen, M.Z.; Lu, Y.; Zhang, L.; Wang, L.; Zhou, Q.Y.; Li, L.; et al. Frequency-modulated continuous waves controlled by space-time-coding metasurface with nonlinearly periodic phases. *Light. Sci. Appl.* **2022**, *11*, 273. [CrossRef] [PubMed]
111. Qian, B.; Zhao, H.; Zhu, X.; Li, P.; Hong, H.; Chu, H.; Guo, Y.X. Nanosecond-level time-domain coding metasurface for radar signal generation. *Nat. Commun.* **2025**, *16*, 10651. [CrossRef] [PubMed]
112. Kozlov, V.; Vovchuk, D.; Ginzburg, P. Direction of arrival deception with time-modulated scatterers. *IEEE Trans. Radar Syst.* **2023**, *1*, 1–10. [CrossRef]
113. Kozlov, V.; Vovchuk, D.; Ginzburg, P. Radar range deception with time-modulated scatterers. *IEEE Trans. Antennas Propag.* **2023**, *71*, 4486–4491. [CrossRef]

114. Ding, C.; Mu, H.; Meng, Y.; Zhao, M.; Zhang, Y.; Cai, T.; Meng, F.; Wang, J. Time-modulated metasurface-assisted moving target jamming for synthetic aperture radar. *IEEE Trans. Microw. Theory Tech.* **2025**, *73*, 4191–4203. [CrossRef]
115. Hu, X.; Xu, W.; Fan, Q.; Yue, T.; Yan, F.; Lu, Y.; Xu, T. Metasurface-based computational imaging: A review. *Adv. Photonics* **2024**, *6*, 014002. [CrossRef]
116. Saigre-Tardif, C.; Faqiri, R.; Zhao, H.; Li, L.; del Hougne, P. Intelligent Meta-Imagers: From Compressed to Learned Sensing. *Appl. Phys. Rev.* **2022**, *9*, 011314. [CrossRef]
117. Cheng, Q.; Ihalage, A.A.; Liu, Y.; Hao, Y. Compressive sensing radar imaging with convolutional neural networks. *IEEE Access* **2020**, *8*, 212917–212926. [CrossRef]
118. Diebold, A.V.; Pulido-Mancera, L.; Sleasman, T.; Boyarsky, M.; Imani, M.F.; Smith, D.R. Generalized range migration algorithm for synthetic aperture radar image reconstruction of metasurface antenna measurements. *J. Opt. Soc. Am. B* **2017**, *34*, 2610–2623. [CrossRef]
119. Hoang, T.V.; Fusco, V.; Fromenteze, T.; Yurduseven, O. Computational polarimetric imaging using two-dimensional dynamic metasurface apertures. *IEEE Open J. Antennas Propag.* **2021**, *2*, 488–497. [CrossRef]
120. Venkatesh, S.; Sturm, D.; Lu, X.; Lang, R.J.; Sengupta, K. Origami Microwave Imaging Array: Metasurface Tiles on a Shape-Morphing Surface for Reconfigurable Computational Imaging. *Adv. Sci.* **2022**, *9*, 2105016. [CrossRef] [PubMed]
121. Martinez, A.O.; De Carvalho, E.; Nielsen, J.Ø. Towards very large aperture massive MIMO: A measurement based study. In *Proceedings of the 2014 IEEE Globecom Workshops (GC Wkshps)*; IEEE: New York, NY, USA, 2014; pp. 281–286.
122. Sayeed, A.; Behdad, N. Continuous aperture phased MIMO: Basic theory and applications. In *Proceedings of the 2010 48th Annual Allerton Conference on Communication, Control, and Computing (Allerton)*; IEEE: New York, NY, USA, 2010; pp. 1196–1203.
123. Pizzo, A.; Marzetta, T.L.; Sanguinetti, L. Degrees of freedom of holographic MIMO channels. In *Proceedings of the 2020 IEEE 21st International Workshop on Signal Processing Advances in Wireless Communications (SPAWC)*; IEEE: New York, NY, USA, 2020; pp. 1–5.
124. Liu, R.; Li, M.; Luo, H.; Liu, Q.; Swindlehurst, A.L. Integrated sensing and communication with reconfigurable intelligent surfaces: Opportunities, applications, and future directions. *IEEE Wirel. Commun.* **2023**, *30*, 50–57. [CrossRef]
125. Chen, X.Q.; Zhang, L.; Zheng, Y.N.; Liu, S.; Huang, Z.R.; Liang, J.C.; Di Renzo, M.; Galdi, V.; Cui, T.J. Integrated sensing and communication based on space-time-coding metasurfaces. *Nat. Commun.* **2025**, *16*, 1836. [CrossRef] [PubMed]
126. Meng, X.; Liu, F.; Lu, S.; Chepuri, S.P.; Masouros, C. RIS-assisted integrated sensing and communications: A subspace rotation approach. In *Proceedings of the 2023 IEEE Radar Conference (RadarConf23)*; IEEE: New York, NY, USA, 2023; pp. 1–6.
127. Zhang, J.A.; Rahman, M.L.; Wu, K.; Huang, X.; Guo, Y.J.; Chen, S.; Yuan, J. Enabling joint communication and radar sensing in mobile networks—A survey. *IEEE Commun. Surv. Tutor.* **2021**, *24*, 306–345. [CrossRef]
128. Liu, R.; Li, M.; Liu, Y.; Wu, Q.; Liu, Q. Joint transmit waveform and passive beamforming design for RIS-aided DFRC systems. *IEEE J. Sel. Top. Signal Process.* **2022**, *16*, 995–1010. [CrossRef]
129. Sun, Z.; Zhang, L.; Chen, X.Q.; Xu, H.; Xiao, G.; Zheng, Y.N.; Wu, Y.; Liu, Z.; Fu, H.; Zhou, X.; et al. Anti-radar based on metasurface. *Nat. Commun.* **2025**, *16*, 7258. [CrossRef] [PubMed]
130. Balci, O.; Polat, E.O.; Kakenov, N.; Kocabas, C. Graphene-enabled electrically switchable radar-absorbing surfaces. *Nat. Commun.* **2015**, *6*, 6628. [CrossRef] [PubMed]
131. Sleasman, T.; Boyarsky, M.; Pulido-Mancera, L.; Fromenteze, T.; Imani, M.F.; Reynolds, M.S.; Smith, D.R. Experimental synthetic aperture radar with dynamic metasurfaces. *IEEE Trans. Antennas Propag.* **2017**, *65*, 6864–6877. [CrossRef]
132. Su, J.; He, H.; Lu, Y.; Yin, H.; Liu, G.; Li, Z. Ultrawideband radar cross-section reduction by a metasurface based on defect lattices and multiwave destructive interference. *Phys. Rev. Appl.* **2019**, *11*, 044088. [CrossRef]
133. Wu, R.Y.; Wu, L.W.; He, S.; Liu, S.; Cui, T.J. Programmable metamaterials. *Program. Mater.* **2023**, *1*, e4. [CrossRef]
134. Lou, Y.; Deng, X.H.; Geng, J.; Zhu, S.; Liu, Y.; Zhang, Y.; Bao, Y.; Hu, P. Design of metasurface structures compatible with multiple detection methods for stealth applications. *Phys. Lett. A* **2025**, *544*, 130487. [CrossRef]
135. Zhang, L.; Wu, R.Y.; Bai, G.D.; Wu, H.T.; Ma, Q.; Chen, X.Q.; Cui, T.J. Transmission-reflection-integrated multifunctional coding metasurface for full-space controls of electromagnetic waves. *Adv. Funct. Mater.* **2018**, *28*, 1802205. [CrossRef]
136. Dai, J.Y.; Zhao, J.; Cheng, Q.; Cui, T.J. Independent control of harmonic amplitudes and phases via a time-domain digital coding metasurface. *Light. Sci. Appl.* **2018**, *7*, 90. [CrossRef] [PubMed]
137. Liu, S.; Wang, J.; Ma, Y.; Sui, R.; Feng, D. Radar target HRRP modulation utilizing multifrequency time-varying metasurface. *IEEE Trans. Microw. Theory Tech.* **2025**, *73*, 9495–9508. [CrossRef]
138. Fang, X.; Li, M.; Zhu, Y.; Ramaccia, D.; Toscano, A.; Bilotti, F.; Ding, D. Suppressing the false targets by time-modulated metasurface with pseudorandom-coded electromagnetic radar fields. *IEEE Trans. Microw. Theory Tech.* **2025**, *73*, 5431–5442. [CrossRef]
139. Ding, F.; Chen, Y.; Bozhevolnyi, S.I. Metasurface-based polarimeters. *Appl. Sci.* **2018**, *8*, 594. [CrossRef]
140. Richards, M.A. *Fundamentals of Radar Signal Processing*; McGraw-Hill: New York, NY, USA, 2005.
141. Zhou, J.; Ding, D.; Li, M. Low probability of intercept DoA estimation using space-time-modulated metasurfaces. *IEEE Trans. Microw. Theory Tech.* **2026**, *74*, 2913–2924. [CrossRef]

142. Wang, X.; Caloz, C. Spread-spectrum selective camouflaging based on time-modulated metasurface. *IEEE Trans. Antennas Propag.* **2020**, *69*, 286–295. [CrossRef]
143. Levanon, N.; Mozeson, E. *Radar Signals*; John Wiley & Sons: Hoboken, NJ, USA, 2004.
144. Li, W.; Zheng, X.; Ren, P. Filter bank multi-carrier waveform design for low probability of intercepting joint radar and communication system. *J. Radars* **2023**, *12*, 287–296. [CrossRef]
145. Dai, J.Y.; Tang, W.; Yang, L.X.; Li, X.; Chen, M.Z.; Ke, J.C.; Cheng, Q.; Jin, S.; Cui, T.J. Realization of multi-modulation schemes for wireless communication by time-domain digital coding metasurface. *IEEE Trans. Antennas Propag.* **2019**, *68*, 1618–1627. [CrossRef]
146. Chittur Subramanianprasad, P. Machine Learning for Design and Optimization of Coding Metasurfaces. Ph.D. Thesis, Queen Mary University of London, London, UK, 2025.
147. Ma, Q.; Liu, C.; Xiao, Q.; Gu, Z.; Gao, X.; Li, L.; Cui, T.J. Information metasurfaces and intelligent metasurfaces. *Photonics Insights* **2022**, *1*, R01. [CrossRef]
148. Qian, C.; Zheng, B.; Shen, Y.; Jing, L.; Li, E.P.; Shen, L.; Chen, H. Deep-learning-enabled self-adaptive microwave cloak without human intervention. *Nat. Photonics* **2020**, *14*, 383–390. [CrossRef]
149. Ma, Q.; Bai, G.D.; Jing, H.B.; Yang, C.; Li, L.; Cui, T.J. Smart metasurface with self-adaptively reprogrammable functions. *Light. Sci. Appl.* **2019**, *8*, 98. [CrossRef] [PubMed]
150. Zhang, G.; Sui, S.; Wang, A.; Wang, J. Coding Metasurface for Radar Cross Section Reduction. In *Proceedings of the 2020 IEEE 3rd International Conference of Safe Production and Informatization (IICSPI)*; IEEE: New York, NY, USA, 2020; pp. 52–55.
151. Huang, C.; Zappone, A.; Alexandropoulos, G.C.; Debbah, M.; Yuen, C. Reconfigurable intelligent surfaces for energy efficiency in wireless communication. *IEEE Trans. Wirel. Commun.* **2019**, *18*, 4157–4170. [CrossRef]
152. Liu, F.; Tsilipakos, O.; Pitilakis, A.; Tasolamprou, A.C.; Mirmoosa, M.S.; Kantartzis, N.V.; Kwon, D.H.; Georgiou, J.; Kossifos, K.; Antoniades, M.A.; et al. Intelligent metasurfaces with continuously tunable local surface impedance for multiple reconfigurable functions. *Phys. Rev. Appl.* **2019**, *11*, 044024. [CrossRef]
153. Chen, Y.; Lu, L.; Karniadakis, G.E.; Dal Negro, L. Physics-informed neural networks for inverse problems in nano-optics and metamaterials. *Opt. Express* **2020**, *28*, 11618–11633. [CrossRef] [PubMed]
154. Liaskos, C.; Nie, S.; Tsioliaridou, A.; Pitsillides, A.; Ioannidis, S.; Akyildiz, I.F. A new wireless communication paradigm through software-controlled metasurfaces. *IEEE Commun. Mag.* **2018**, *56*, 162–169. [CrossRef]
155. Di Renzo, M.; Zappone, A.; Debbah, M.; Alouini, M.S.; Yuen, C.; de Rosny, J.; Tretyakov, S.A. Smart radio environments empowered by reconfigurable intelligent surfaces: How it works, state of research, and the road ahead. *IEEE J. Sel. Areas Commun.* **2020**, *38*, 2450–2525. [CrossRef]
156. Haykin, S.; Xue, Y.; Setoodeh, P. Cognitive radar: Step toward bridging the gap between neuroscience and engineering. *Proc. IEEE* **2012**, *100*, 3102–3130. [CrossRef]
157. Khaleghi, B.; Khamis, A.; Karray, F.O.; Razavi, S.N. Multisensor data fusion: A review of the state-of-the-art. *Inf. Fusion* **2013**, *14*, 28–44. [CrossRef]
158. Qiu, T.; An, Q.; Wang, J.; Wang, J.; Qiu, C.W.; Li, S.; Lv, H.; Cai, M.; Wang, J.; Cong, L.; et al. Vision-driven metasurfaces for perception enhancement. *Nat. Commun.* **2024**, *15*, 1631. [CrossRef] [PubMed]
159. González-Prelcic, N.; Méndez-Rial, R.; Heath, R.W. Radar aided beam alignment in mmWave V2I communications supporting antenna diversity. In *Proceedings of the 2016 Information Theory and Applications Workshop (ITA)*; IEEE: New York, NY, USA, 2016; pp. 1–7.
160. Durrant-Whyte, H.; Henderson, T.C. Multisensor data fusion. In *Springer Handbook of Robotics*; Springer: Berlin/Heidelberg, Germany, 2016; pp. 867–896.
161. Zhao, Y.; Alù, A. Manipulating light polarization with ultrathin plasmonic metasurfaces. *Phys. Rev. B—Condensed Matter Mater. Phys.* **2011**, *84*, 205428. [CrossRef]
162. Di Renzo, M.; Ntontin, K.; Song, J.; Danufane, F.H.; Qian, X.; Lazarakis, F.; de Rosny, J.; Phan-Huy, D.T.; Simeone, O.; Zhang, R.; et al. Reconfigurable intelligent surfaces vs. relaying: Differences, similarities, and performance comparison. *IEEE Open J. Commun. Soc.* **2020**, *1*, 798–807. [CrossRef]
163. Siddiqi, M.Z.; Mir, T. Reconfigurable intelligent surface-aided wireless communications: An overview. *Intell. Converg. Netw.* **2022**, *3*, 33–63. [CrossRef]
164. Liaskos, C.; Mamatas, L.; Pourdamghani, A.; Tsioliaridou, A.; Ioannidis, S.; Pitsillides, A.; Schmid, S.; Akyildiz, I.F. Software-defined reconfigurable intelligent surfaces: From theory to end-to-end implementation. *Proc. IEEE* **2022**, *110*, 1466–1493. [CrossRef]
165. Liang, Y.C.; Long, R.; Zhang, Q.; Chen, J.; Cheng, H.V.; Guo, H. Large intelligent surface/antennas (LISA): Making reflective radios smart. *J. Commun. Inf. Netw.* **2019**, *4*, 40–50. [CrossRef]
166. Liu, L.; Huang, Y.F.; Zhang, H.C. Design of a Wide-Angle and Polarization-Free 1-Bit Programmable Metasurface. *Front. Mater.* **2022**, *9*, 933163. [CrossRef]

167. Xu, L.; Zhang, X.G.; Li, Q.Y.; Jiang, W.X.; Cui, T.J. Programmable metasurfaces with high angular stability for arbitrarily-polarized obliquely-incident waves. *J. Phys. D Appl. Phys.* **2024**, *57*, 375301. [CrossRef]
168. Su, J.; Lu, Y.; Zhang, H.; Li, Z.; Yang, Y.L.; Che, Y.; Qi, K. Ultra-wideband, Wide Angle and Polarization-insensitive Specular Reflection Reduction by Metasurface Based on Parameter-adjustable Meta-atoms. *Sci. Rep.* **2017**, *7*, 42283. [CrossRef] [PubMed]
169. Su, P.; Zhao, Y.; Jia, S.; Shi, W.; Wang, H. An Ultra-wideband and Polarization-independent Metasurface for Radar Cross Section Reduction. *Sci. Rep.* **2016**, *6*, 20387. [CrossRef] [PubMed]
170. Guo, Z.; Zhou, Y.; Yang, H.; Li, S.; Li, T.; Cao, X. Programmable Multifunctional Metasurface for Polarization, Phase, and Amplitude Manipulation. *Opt. Express* **2023**, *31*, 35086–35099. [CrossRef] [PubMed]
171. Sun, S.; Yang, K.Y.; Wang, C.M.; Juan, T.K.; Chen, W.T.; Liao, C.Y.; He, Q.; Xiao, S.; Kung, W.T.; Guo, G.Y.; et al. High-efficiency broadband anomalous reflection by gradient meta-surfaces. *Nano Lett.* **2012**, *12*, 6223–6229. [CrossRef] [PubMed]
172. Mehdipour, A.; Wong, J.W.; Eleftheriades, G.V. Beam-squinting reduction of leaky-wave antennas using Huygens metasurfaces. *IEEE Trans. Antennas Propag.* **2015**, *63*, 978–992. [CrossRef]
173. Zetterstrom, O.; Pucci, E.; Padilla, P.; Wang, L.; Quevedo-Teruel, O. Low-dispersive leaky-wave antennas for mmWave point-to-point high-throughput communications. *IEEE Trans. Antennas Propag.* **2019**, *68*, 1322–1331. [CrossRef]
174. Chen, W.T.; Zhu, A.Y.; Sanjeev, V.; Khorasaninejad, M.; Shi, Z.; Lee, E.; Capasso, F. A broadband achromatic metalens for focusing and imaging in the visible. *Nat. Nanotechnol.* **2018**, *13*, 220–226. [CrossRef] [PubMed]
175. Ding, X.; Monticone, F.; Zhang, K.; Zhang, L.; Gao, D.; Nawaz Burokur, S.; de Lustrac, A.; Wu, Q.; Qiu, C.W.; Alù, A. Ultrathin Pancharatnam–Berry metasurface with maximal cross-polarization efficiency. *Adv. Mater.* **2015**, *27*, 1195–1200. [CrossRef] [PubMed]
176. Shaltout, A.; Kildishev, A.; Shalaev, V. Time-varying metasurfaces and Lorentz non-reciprocity. *Opt. Mater. Express* **2015**, *5*, 2459–2467. [CrossRef]
177. Shlezinger, N.; Dicker, O.; Eldar, Y.C.; Yoo, I.; Imani, M.F.; Smith, D.R. Dynamic metasurface antennas for uplink massive MIMO systems. *IEEE Trans. Commun.* **2019**, *67*, 6829–6843. [CrossRef]
178. Wang, H.; Shlezinger, N.; Eldar, Y.C.; Jin, S.; Imani, M.F.; Yoo, I.; Smith, D.R. Dynamic metasurface antennas for MIMO-OFDM receivers with bit-limited ADCs. *IEEE Trans. Commun.* **2020**, *69*, 2643–2659. [CrossRef]
179. Chouhan, B.S.; Nawaz, A.; Das, A.; Rohith, K.M.; Ahmad, A.; Kumar, G. Machine learning-driven ultra-broadband terahertz multilayer metamaterial. *J. Light. Technol.* **2024**, *43*, 2734–2744. [CrossRef]
180. Alexandropoulos, G.C.; Stylianopoulos, K.; Huang, C.; Yuen, C.; Bennis, M.; Debbah, M. Pervasive machine learning for smart radio environments enabled by reconfigurable intelligent surfaces. *Proc. IEEE* **2022**, *110*, 1494–1525. [CrossRef]
181. Shlezinger, N.; Alexandropoulos, G.C.; Imani, M.F.; Eldar, Y.C.; Smith, D.R. Dynamic metasurface antennas for 6G extreme massive MIMO communications. *IEEE Wirel. Commun.* **2021**, *28*, 106–113. [CrossRef]
182. Dai, J.Y.; Tang, W.; Chen, M.Z.; Chan, C.H.; Cheng, Q.; Jin, S.; Cui, T.J. Wireless communication based on information metasurfaces. *IEEE Trans. Microw. Theory Tech.* **2021**, *69*, 1493–1510. [CrossRef]
183. Guo, T.; Argyropoulos, C. Nonreciprocal transmission of electromagnetic waves with nonlinear active plasmonic metasurfaces. *Phys. Rev. B* **2022**, *106*, 235418. [CrossRef]
184. Chen, J.; Hu, S.; Zhu, S.; Li, T. Metamaterials: From fundamental physics to intelligent design. *Interdiscip. Mater.* **2023**, *2*, 5–29. [CrossRef]
185. Ma, Q.; Cui, T.J. Information metamaterials: Bridging the physical world and digital world. *PhotoniX* **2020**, *1*, 1. [CrossRef]
186. Silva, A.; Monticone, F.; Castaldi, G.; Galdi, V.; Alu, A.; Engheta, N. Performing mathematical operations with metamaterials. *Science* **2014**, *343*, 160–163. [CrossRef] [PubMed]
187. Li, L.; Shuang, Y.; Ma, Q.; Li, H.; Zhao, H.; Wei, M.; Liu, C.; Hao, C.; Qiu, C.W.; Cui, T.J. Intelligent metasurface imager and recognizer. *Light. Sci. Appl.* **2019**, *8*, 97. [CrossRef] [PubMed]
188. Li, L.; Zhao, H.; Liu, C.; Li, L.; Cui, T.J. Intelligent metasurfaces: Control, communication and computing. *eLight* **2022**, *2*, 7. [CrossRef]
189. Wei, M.; Zhao, H.; Galdi, V.; Li, L.; Cui, T.J. Metasurface-enabled smart wireless attacks at the physical layer. *Nat. Electron.* **2023**, *6*, 610–618. [CrossRef]
190. Hu, X.; Zhong, C.; Zhang, Y.; Chen, X.; Zhang, Z. Location information aided multiple intelligent reflecting surface systems. *IEEE Trans. Commun.* **2020**, *68*, 7948–7962. [CrossRef]

Disclaimer/Publisher's Note: The statements, opinions and data contained in all publications are solely those of the individual author(s) and contributor(s) and not of MDPI and/or the editor(s). MDPI and/or the editor(s) disclaim responsibility for any injury to people or property resulting from any ideas, methods, instructions or products referred to in the content.